International Journal of Coal Geology 289 (2024) 104546

Contents lists available at ScienceDirect

International Journal of Coal Geology

journal homepage: www.elsevier.com/locate/coal

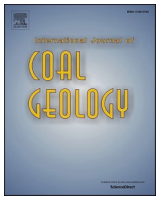

Understanding the burial history and the hydrocarbon potential of the late Paleozoic Claromecó foreland Basin (Southwestern Gondwana, Argentina) by combining organic geochemistry, organic petrology, and thermal modeling

María Belén Febbo [a,b,*], Silvia Omodeo-Salé [a], Andrea Moscariello [a]

[a] University of Geneva, Department of Earth Sciences, 1205 Geneva, Switzerland
[b] German Research Centre for Geosciences (GFZ), Helmholtz Centre, 14473 Potsdam, Germany

ARTICLE INFO

Keywords:
Thermal history
Tunas formation
Gondwana coals
Permian
Coalification degree
Vitrinite reflectance

ABSTRACT

The Claromecó foreland Basin (Carboniferous–Permian; southern Buenos Aires province, Argentina) is key to understanding the paleotectonic evolution of the southwestern Gondwana margin and is relevant to energy resource exploration. This study reconstructs the thermal and burial history of the Claromecó Basin by integrating geochemical data, organic petrology, and thermal modeling techniques. Cores samples of the Tunas Formation (Pillahuincó Group, Early Permian) were studied. A 1D thermal model was constructed, calibrated with vitrinite reflectance measurements (VRo %), and corroborated with fluid inclusion and apatite fission track data from previous studies. Rock-Eval pyrolysis results show TOC% values ranging from 0.13 to 60.35 wt%. The Hydrogen index (HI < 50 mg HC/g TOC) and Oxygen index (OI < 50 mg CO_2/g TOC) indicate the dominance of Type III and Type IV kerogens, most likely resulting from the thermal maturation of an original Type III kerogen. Petrologic observations confirm the presence of macerals from the inertinite group, as well as minor amounts of vitrinite and liptinite. The Tmax displays a temperature range mostly from 460 to 610 °C. The VRo % values range from 1.5 to 2.0%. Geochemical data combined with VRo % measurements confirm a late catagenesis to metagenesis stage within the wet to dry gas window for coals and organic-rich strata.

In order to constrain the thermal evolution of the basin infill, different scenarios were tested by varying the heat flow and the missing section thickness associated with the uplift and erosion of the basin (Permian–Cenozoic unconformity). The best calibration results were obtained with an erosion thickness of 3000 up to 4200 m and paleo heat flow peaks of either 60 or 80 mW/m^2 during the Lower Permian–Lower Cretaceous. The Tunas Formation was deposited and buried during the Permian–Triassic (Gondwanides Orogeny phase), reaching a maximum temperature of 180 °C. The results obtained by combining geochemical analysis, organic petrology, and thermal modeling techniques indicate that the coal beds of the Tunas Formation could have a current potential as gas-prone source rocks. Despite that, the hydrocarbon generation capacity of coal levels is currently low due to the high percentage of residual (Type IV) kerogen. Further research could help clarify if the hydrocarbons potentially expelled by these source rocks have been lost due to migration or could be trapped somewhere in the basin.

1. Introduction

The Carboniferous–Permian Claromecó foreland Basin (southern Buenos Aires province, Argentina; Fig. 1a) is key to understanding the paleotectonic evolution of southwestern Gondwana and the tectonic events that led to the formation of Pangea in the Late Paleozoic–Triassic (Ramos, 1984, 2008; Tomezzoli, 2001, 2012; Pángaro and Ramos, 2012; Arzadún et al., 2016, 2021; Tomezzoli et al., 2018; Prezzi et al., 2018). The basin covers an area of approximately 65,000 km^2, extending from the Sierras Australes fold and thrust belt to the Argentinean continental shelf (37°– 40° S and 61°– 58° W, Fig. 1). The study of this basin is relevant for exploring energy resources in Argentina due to the presence

* Corresponding author at: University of Geneva, Department of Earth Sciences, 1205 Geneva, Switzerland.
E-mail addresses: febbo@gfz-potsdam.de (M.B. Febbo), Silvia.OmodeoSale@unige.ch (S. Omodeo-Salé), Andrea.Moscariello@unige.ch (A. Moscariello).

https://doi.org/10.1016/j.coal.2024.104546
Received 12 March 2024; Received in revised form 2 June 2024; Accepted 2 June 2024
Available online 6 June 2024

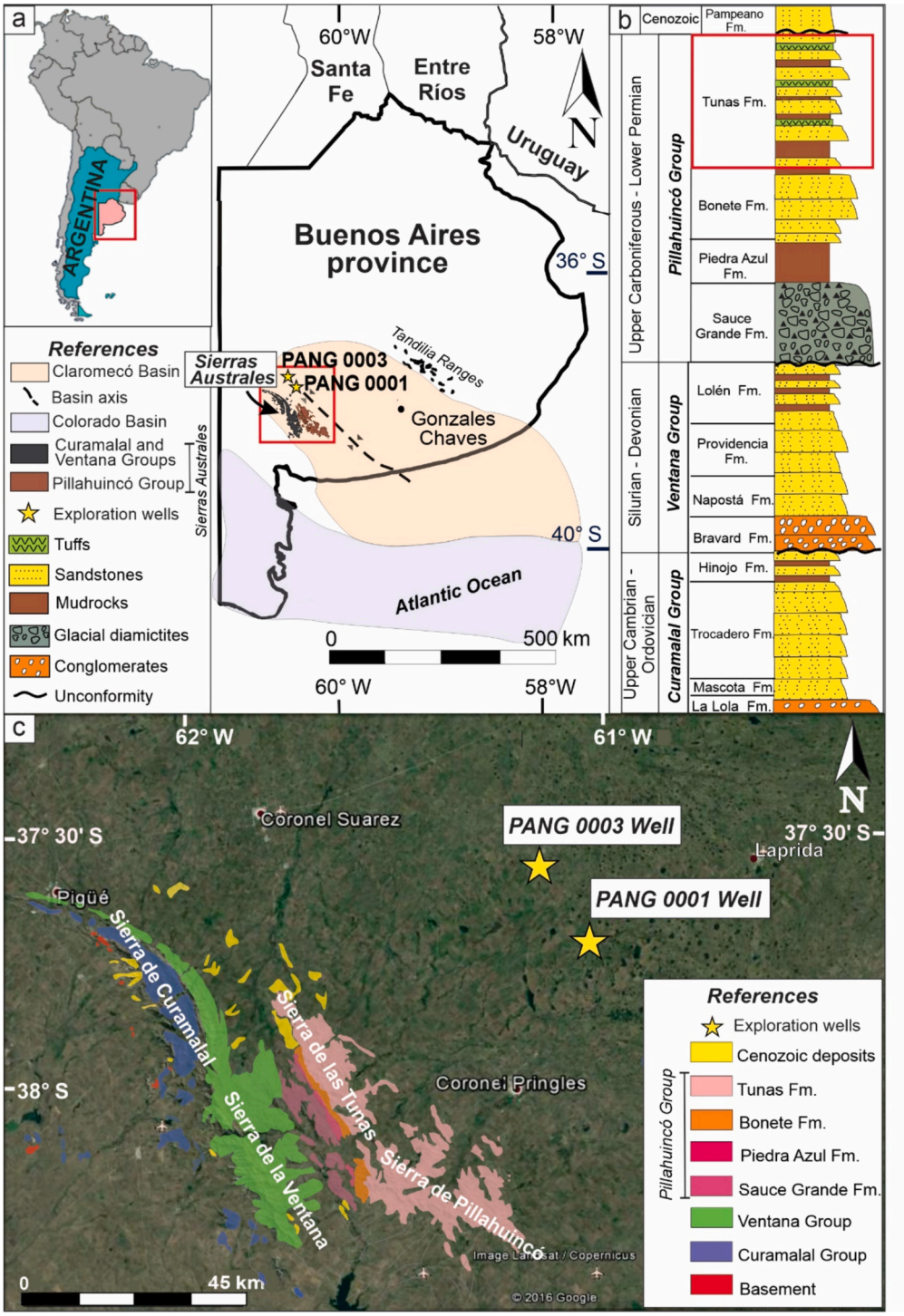

Fig. 1. a) Location of the Claromecó Basin, Sierras Australes fold and thrust belt, PANG 0001, and PANG 0003 wells, as well as Mesozoic Colorado Basin; **b)** Stratigraphic column of the Paleozoic sedimentary succession of the Sierras Australes and the Claromecó Basin, based on Harrington (1947, 1970), Buggisch (1987), and Ramos et al. (2014); **c)** Geological map of the Sierras Australes fold and thrust belt showing the Tunas Formation outcrops (Suero, 1972) and location of the PANG 0001 and PANG 0003 wells.

of subsurface coal beds and potential gas accumulations (Lesta and Sylwan, 2005; Arzadún et al., 2017; Zavala et al., 2019; López-Gamundi and Rossello, 2021; Febbo et al., 2022a, 2023). In addition, in recent years, the coal seams of Claromecó Basin have been identified as potential targets for CO_2 capture and storage (CCS; Grasetti et al., 2022). Therefore, it is relevant to perform an exhaustive study of the coal deposits in this area, as the coal sorption capacity depends on its total organic carbon content (TOC), coal rank (degree of coalification), and mineral matter content (Yu et al., 2007). Although the Claromecó Basin holds significant scientific and economic importance, its geological evolution remains poorly understood due to the lack of Paleozoic outcrops in the foreland area and the scattered and scarce subsurface data available.

This work aims to reconstruct the thermal and burial history of the Claromecó Basin by integrating geochemical data, organic petrology, and thermal modeling techniques. Sedimentary records of the Tunas

Formation, obtained from the PANG 0001 and PANG 0003 wells (Figs. 1a–c), were analyzed. The Tunas Formation (Early Permian, Figs. 1b, c; Harrington, 1947) is the youngest unit of the Pillahuincó Group and represents the last stage of the Late Paleozoic basin filling. The sedimentary deposits of this unit recorded the syntectonic deformation that occurred during the Late Paleozoic Gondwanides Orogeny (Tomezzoli, 2001; Arzadún et al., 2016, 2021; Febbo et al., 2021). Therefore, studying the burial history of the Tunas Formation contributes to a better understanding of the paleotectonic evolution of the SW Gondwana margin, which is still under debate. The Tunas Formation subsurface records from the PANG 0001 and 0003 wells, drilled by Rio Tinto Mining S.A. in 2010, have been studied using a multidisciplinary approach: thermochronology (Arzadún et al., 2020), sedimentology (Zavala et al., 2019), palynology (Di Nardo et al., 2022), mechanical stratigraphy (Choque et al., 2021, 2022), geophysics (Febbo et al., 2021), and diagenesis (Febbo et al., 2023). The hydrocarbon potential of the Claromecó Basin was defined by analyzing coal deposits of the Tunas Formation. The TOC% content ranging from 0.5 to 53.9% and vitrinite reflectance (VRo %) values ranging from 1.3 to 2.4% indicate that the coal-bearing layers have gas-prone source rock potential, with a maturity stage within the wet to dry gas window (Arzadún et al., 2017; Febbo et al., 2022a).

In the present study, a more detailed geochemical screening and organic petrologic analyses were carried out for the coals and organic-rich strata of the Tunas Formation in PANG 0001 and PANG 0003 wells. Furthermore, 1D models were constructed for these wells, in order to estimate the maximum temperature reached by the sedimentary infill, considering the primary factors that control the temperature in sedimentary basins, such as basin geometry, basin heat flow, burial, erosion, facies distribution, and fluid migration (Tissot and Welte, 1984; Tissot et al., 1987; Littke et al., 2008). Thermal modeling results were used to determine the tectono-stratigraphic evolution of the basin infill (burial, uplift, exhumation, and erosion periods) and to define the coalification degree of the Permian coal deposits. Finally, the latter results were used to assess the hydrocarbon potential of the Claromecó Basin.

2. Geological setting

The study area is located in the northwestern portion of the Claromecó foreland Basin in southern Buenos Aires province, Argentina (Figs. 1a, c). The basin was formed along the southwestern Gondwana margin during the late Paleozoic (Keidel, 1916; Ramos, 1984) and was filled by sedimentary deposits of the Pillahuincó Group (Carboniferous–early Permian in age, Figs. 1 a–c; Harrington, 1947). The Paleozoic basin extends from the Sierras Australes to the east-northeast area, limiting with the Tandilia Ranges (Fig. 1a). Southward, the basin extends towards the Argentinean continental shelf where it forms the pre-rift basement of the Colorado Basin (Fig. 1a; Fryklund et al., 1996; Lesta and Sylwan, 2005; Pángaro and Ramos, 2012). Gravimetric studies revealed a maximum thickness of 9 to 10.5 km for the sedimentary basin infill (Introcaso, 1982; Kostadinoff and Prozzi, 1998; Kostadinoff, 2007).

2.1. Geodynamic history of the Claromecó Basin

The evolution of the southwestern Gondwana margin in central Argentina is summarized in four major tectonic events: (i) rifting phase during the Early Paleozoic; (ii) passive margin period from the Ordovician to the Devonian; (iii) compressive deformation phase and development of the foreland basin in the Late Paleozoic; and finally, (iv) rifting events and passive margin formation during the Mesozoic (e.g., Rapela et al., 2003, 2007; Kollenz et al., 2017; Vazquez Lucero et al., 2020; Arzadún et al., 2021; Christiansen et al., 2021). The Claromecó Basin was formed in a foreland geodynamic context as a result of the accretion of terranes and microplates to the southwestern margin of Gondwana during the Gondwanides orogeny stage (Late Paleozoic–Early Triassic; Ramos, 1984, 2008; Tomezzoli, 2001, 2012; Pángaro and Ramos, 2012; Ramos and Naipauer, 2014). The Sierras Australes fold and thrust belt was deformed during the collisional stage, while the foreland zone experienced tectonic subsidence. This compressional phase led to the rapid accumulation and subsequent burial of the sedimentary strata in the foreland area from the Late Permian until the Triassic (Kollenz et al., 2017). After the end of the orogeny, generalized extension events affected the SW margin of Gondwana during the Late Triassic–Cretaceous. The Mesozoic rifting involved 3 major events: (i) an initial stage (Late Triassic–Early Jurassic; Lovecchio et al., 2018), related to the extensional reactivation of previously compressive thrusts of the Sierras Australes and the Cape fold belt; (ii) a Syn-Rift stage (Early Jurassic–Early Cretaceous; Mpodozis and Ramos, 2008; Lovecchio et al., 2018), associated with the formation of the Colorado Basin (Fig. 1a); (iii) a Post-Rift stage (Early Cretaceous–Cenozoic; Kollenz et al., 2017; Lovecchio et al., 2018), linked with the Atlantic Ocean break-up. Finally, the passive margin was formed due to the drifting of the South American plate during the opening of the South Atlantic Ocean.

The Mesozoic extensional tectonic events played a crucial role in the exhumation and erosion of the stratigraphic record of the Claromecó Basin. During the *syn*-rift stage, this area acted as the northern flank of the Colorado Basin, which would have resulted in the uplift and exhumation of the basin infill (Arzadún et al., 2020). Thermochronological studies conducted on subsurface samples from the Tunas Formation (PANG 0003 well) indicate a major exhumation period for the basin infill during the Early Cretaceous (Barremian–Aptian, 125.8 ± 10.6 Ma; Arzadún et al., 2020). According to these authors, the uplift was linked to the passive margin exhumation during the drift stage.

2.2. Basin infill

The foreland sedimentary record of the Claromecó Basin comprises the late Paleozoic Pillahuincó Group (Figs. 1a, b; Harrington, 1947, 1970). This group outcrops in the eastern part of the Sierras Australes with a maximum thickness of 2800 m and extends eastward, covered by Cenozoic deposits (Figs. 1b, c). The Pillahuincó Group overlies the Ordovician to Devonian deposits of the Curamalal and Ventana groups (Fig. 1b) and is divided into four formations: Sauce Grande, Piedra Azul, Bonete, and Tunas (Figs. 1b, c; Harrington, 1947). The Sauce Grande Formation (Late Carboniferous; di Pasquo et al., 2008) comprises glaciomarine deposits characterized by diamictites, sandstones, and shales (Andreis et al., 1987). This unit is overlain by shallow marine shales and sandstones from the Piedra Azul and Bonete formations (Early Permian; Harrington, 1947). At the top of the sequence, fine- to medium-grained sandstones interbedded with laminated shales and thin volcanic levels of the Tunas Formation were deposited in deltaic to fluvial environments (Harrington, 1947, 1970; Andreis et al., 1989; Zavala et al., 1993, 2019; López-Gamundi et al., 1995, 2013; Ballivián Justiniano et al., 2020). The Tunas Formation is exposed north of the Sierras de las Tunas and south of the Sierra de Pillahuincó (Fig. 1b), with small isolated outcrops near Gonzales Chaves locality (Fig. 1a; Monteverde, 1937; Furque, 1965; Harrington, 1970; Tomezzoli and Vilas, 1997; Febbo et al., 2022b). The Tunas Formation is only present in the subsurface towards the foreland basin area (PANG 0001 and 0003; Figs. 1a, c). Subsurface records comprise medium- to fine-grained sandstones interbedded with organic-rich shales, heterolites, shales, tuffs, and coal seams. An Early Permian age is assigned to the Tunas Formation unit based on its fossil record (Archangelsky and Cúneo, 1984) and U—Pb zircon ages (Tohver et al., 2008; Alessandretti et al., 2013; López-Gamundi et al., 2013; Arzadún et al., 2018).

3. Samples and methods

To reconstruct the thermal and burial history of the Claromecó Basin, geochemical and petrologic analyses were carried out and combined with the thermal modeling approach. The analytical methods applied

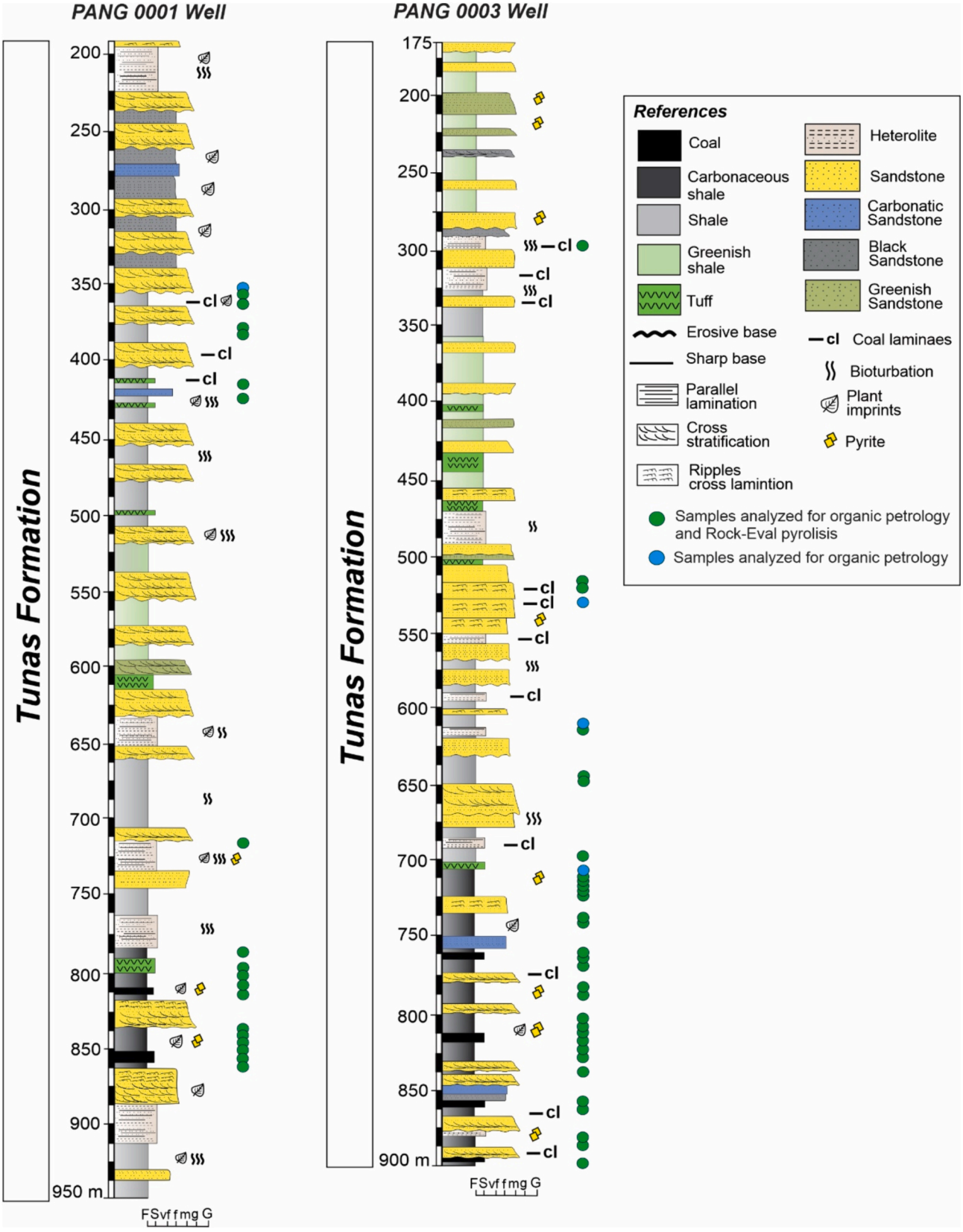

Fig. 2. Sedimentary profiles of the Tunas Formation (PANG 0001 and PANG 0003 wells, Claromecó Basin) and stratigraphic position of core samples used for geochemical (Rock-Eval pyrolysis) and/or organic petrology analyses.

Table 1
Conceptual geological model with depositional and erosional events defined. The Tunas Formation was divided into sub-layers to distinguish the different lithologies that composed this unit.

Age at the top (Ma)	Event/Layer name	Event type	Lithology and percentage (%)
0	Hiatus Cenozoic – 0	Hiatus	–
2	Pampeano	Deposition	Sandstone (100%)
20	Erosion Permian – Cenozoic	Erosion	–
210	Burial Permian – Triassic	Deposition	–
261	Tunas 5	Deposition	Shale (60%) Sandstone (40%)
290	Tunas 4	Deposition	Shale (70%) Sandstone (22%) Organic-rich shale (8%)
291	Tunas 3	Deposition	Shale (70%) Sandstone (20%) Tuff (10%)
292	Tunas 2	Deposition	Shale (65%) Sandstone (30%) Tuff (5%)
293	Tunas 1	Deposition	Shale (60%) Sandstone (30%) Coal (10%)
294	Bonete Fm	Deposition	Sandstone (100%)
296.90	Piedra Azul Fm	Deposition	Shale (100%)
300	Sauce Grande Fm	Deposition	Conglomerate (100%)
323	Hiatus Devonian – Carboniferous	Hiatus	–
358	Ventana Group	Deposition	Quartzite (100%)
453	Hiatus Ordovician – Silurian	Hiatus	–
467	Curamalal Group	Deposition	Quartzite (100%)
497	Hiatus Ordovician – Cambrian	Hiatus	–
509	Basement	Deposition	Granite (100%)
520	End	–	–

include: i) Rock-Eval; ii) maceral analysis; and iii) vitrinite reflectance measurement. The analyzed core samples belong to the Tunas Formation and were collected from the PANG 0001 (S37° 40.8′ 17.0″, W61° 11.30′ 06″) and PANG 0003 wells (S37° 34′ 44.24″, W61° 22′ 12.56″) (Figs. 1a, c). The sedimentary record studied consists of 700 m of fully cored Permian sediments overlain by ~180 m of Cenozoic deposits (Fig. 2). The sedimentary successions consist of medium- to fine-grained greyish to greenish sandstones, interbedded with heterolites, greyish to greenish shales, thin tuff layers, carbonaceous shales, and coals (Fig. 2). Two main intervals of organic-rich fine-grained lithologies were identified: a lower horizon at the base of the wells and an upper horizon at the top. The upper horizon (350–420 m PANG 0001 well and 300–350 m PANG 0003 well; Fig. 2) is characterized by shales and carbonaceous shales with a maximum thickness of 5 cm. The lower horizon (750–800 m PANG 0001 well and 700–850 m PANG 0003 well; Fig. 2) is composed of carbonaceous shales and coals with a maximum thickness of 3.50 m. Representative samples were collected from both intervals to conduct Rock-Eval pyrolysis and organic petrology analyses (Fig. 2). Coal, carbonaceous shales, and shales were differentiated based on their organic matter content (TOC%) obtained from Rock-Eval pyrolisis analysis and the percentage of organic matter vs. mineral matter determined by maceral analysis.

3.1. Rock–Eval analysis

Geochemical analyses were conducted on 49 organic-rich shale and coal samples from the PANG 0001 and 0003 wells (Fig. 2). Rock-Eval pyrolysis studies were conducted to determine the organic matter richness (TOC wt%), estimate the thermal maturity of organic-rich shales and the degree of coalification of coals (Tmax °C), and determine the kerogen type. The analyses were performed at the Institute of Earth Sciences of the University of Lausanne (Switzerland), using a Rock-Eval 6 pyrolizer (Vinci Technologies), on approximately 100 mg crushed sample heated to 600 °C in a helium atmosphere. Several parameters were measured: i) TOC (wt%), total content of organic carbon in the rock; ii) S1 (mg HC/g rock), free hydrocarbons contained in the organic matter; iii) S2 (mg HC/g rock), amount of hydrocarbons formed during the pyrolysis process, which indicates the hydrocarbon generation potential of the rock; iii) S3 (mg CO_2/g rock), amount of CO_2 pyrolyzed; and iv) Tmax (°C), temperature when the S2 peak is recorded (Espitalié et al., 1985a; b; Espitalié et al., 1986). Additionally, source rock parameters, such as Hydrogen index (HI, mg HC/g TOC), Oxygen index (OI, mg CO_2/g TOC), and Production index (PI: S1/(S1 + S2) were calculated to evaluate the kerogen type and the hydrocarbon generation and expulsion potential (Espitalié et al., 1985a, b; Espitalié et al., 1986).

3.2. Organic petrology

Organic petrology analyses were performed on 53 organic-rich shale and coal samples, collected from the cores of the PANG 0001 and 0003 wells (Fig. 2). The polished pellets used for petrologic analyses were prepared as epoxy-impregnated blocks (approximately 2.5 cm × 2.5 cm) according to standard procedures (ISO-7004-2, 2009). The pellets

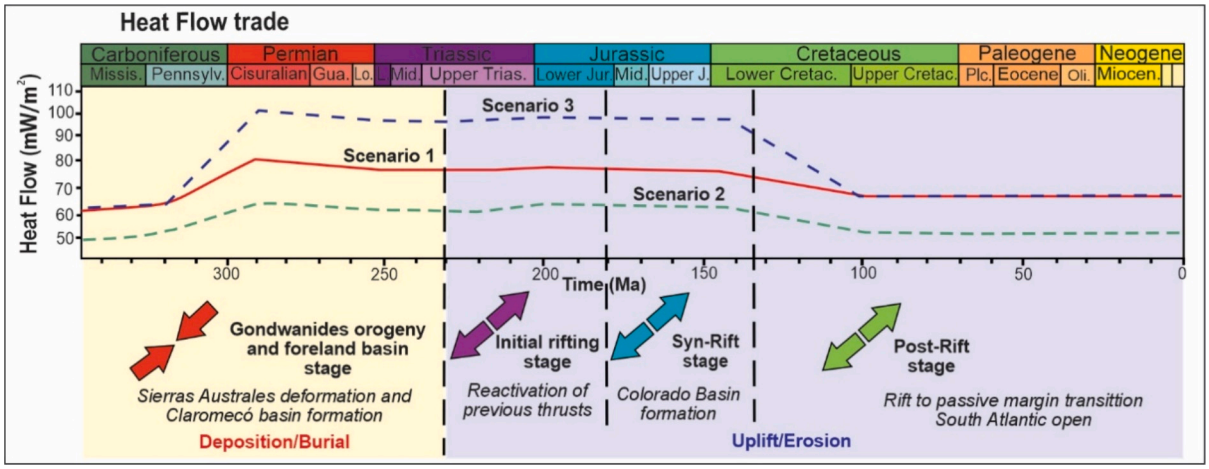

Fig. 3. Paleo heat flow scenarios tested with peaks of 80 mW/m^2 (Scenario 1), 60 mW/m^2 (Scenario 2), and 100 mW/m^2 (Scenario 3) reached from the Permian to the Early Cretaceous. The geodynamic history of the basin was reconstructed based on Pángaro and Ramos (2012), Kollenz et al. (2017), Lovecchio et al. (2018), and Arzadún et al. (2020).

Table 2
Rock-Eval pyrolysis results from analyzed samples from the Tunas Formation.

Well	Sample	Depth	Lithology	TOC [wt %]	HI [mg HC/g TOC]	OI [mg CO_2/g TOC]	Tmax [°C]	S1 [mg HC/g rock]	S2 [mg HC/g rock]	S3	Production Index S1/(S1 + S2)
PANG 0001	C01	863.19	Carb. shale	8.86	18	5	590	0.12	1.59	0.42	0.07
	C03	858	Shale	4.09	14	3	603	0.07	0.56	0.14	0.11
	C04	856.87	Shale	4.16	15	4	599	0.07	0.63	0.17	0.10
	C04A	855.5	Carb. shale	9.32	14	2	603	0.06	1.30	0.22	0.05
	C05	853.5	Shale	0.57	17	13	596	0.01	0.10	0.07	0.13
	C06	850	Shale	1.49	15	11	600	0.03	0.22	0.16	0.12
	C07	847.5	Shale	3.18	11	4	604	0.04	0.35	0.13	0.11
	C08	813.4	Carb. shale	7.14	10	3	602	0.08	0.75	0.18	0.09
	C08A	812	Coal	60.35	10	1	600	0.11	6.18	0.67	0.02
	C09	810.6	Carb. shale	20.17	16	2	598	0.12	3.17	0.41	0.04
	C10	801.8	Carb. shale	27.91	16	3	597	0.23	4.33	0.91	0.05
	C11	790.6	Coal	60.33	13	1	585	0.20	7.92	0.74	0.03
	C13	709.35	Shale	2.97	14	7	532	0.25	0.42	0.22	0.38
	C14	420.8	Shale	2.73	17	5	521	0.07	0.45	0.13	0.13
	C15	418.6	Shale	3.00	18	8	519	0.16	0.54	0.24	0.23
	C16	358.82	Shale	1.83	11	7	498	0.06	0.21	0.12	0.21
	C17	358.44	Shale	0.48	20	23	462	0.02	0.09	0.11	0.19
	C18	355	Shale	0.13	31	41	532	0.01	0.04	0.06	0.26
	C19	354.7	Coal	55.53	20	1	499	0.10	11.28	0.82	0.01
	M6	896.3	Shale	0.95	10	6	605	0.02	0.09	0.06	0.17
PANG 0003	M10	893.05	Carb. shale	20.95	10	3	607	0.40	2.11	0.54	0.16
	M13	888.4	Shale	4.41	11	6	608	0.05	0.47	0.27	0.10
	M39A	853.28	Carb. shale	30.59	3	4	608	0.12	0.88	1.18	0.12
	M43	850.54	Coal	50.91	6	2	607	0.70	3.30	0.81	0.18
	M49	842.4	Carb. shale	42.45	6	2	607	0.34	2.72	0.65	0.11
	M58	832.3	Carb. shale	17.17	5	2	608	0.17	0.81	0.38	0.17
	M61	829.47	Shale	0.33	43	29	476	0.02	0.14	0.09	0.13
	M76	810.34	Shale	0.32	25	17	466	0.01	0.08	0.06	0.14
	M79	809.03	Shale	3.69	8	6	606	0.03	0.28	0.24	0.08
	M80	807	Carb. shale	43.25	6	2	607	0.08	2.52	0.67	0.03
	M80A	807.75	Carb. shale	37.23	7	2	607	0.17	2.65	0.68	0.06
	M93	798	Coal	58.64	7	1	606	0.23	4.26	0.75	0.05
	M95	797.15	Carb. shale	18.47	6	2	607	0.14	1.03	0.39	0.12
	M97A	786.25	Coal	52.33	6	2	607	0.21	3.01	0.99	0.06
	M103	778.53	Shale	0.81	16	32	604	0.03	0.13	0.26	0.17
	M110	770.5	Carb. shale	44.38	5	2	608	0.28	2.05	0.82	0.12
	M113	768.14	Shale	0.68	12	21	604	0.01	0.08	0.14	0.15
	M120	752.77	Carb. shale	19.19	9	2	606	0.13	1.74	0.35	0.07
	M127	743.86	Shale	0.18	39	41	477	0.01	0.07	0.08	0.13
	M139	729.56	Carb. shale	8.30	9	3	602	0.16	0.71	0.25	0.19
	M146	720.31	Carb. shale	16.74	11	4	606	0.22	1.79	0.69	0.11
	M149	714.53	Carb. shale	45.44	4	2	607	0.09	1.65	0.70	0.05
	M153	707.3	Carb. shale	20.06	8	2	604	0.22	1.53	0.45	0.13
	M167	693.08	Shale	4.61	7	4	604	0.04	0.31	0.20	0.12
	M196	634.2	Coal	60.71	11	1	530	0.28	6.58	0.89	0.04
	M204	618.55	Shale	0.42	19	32	481	0.02	0.08	0.14	0.24
	M205	540.4	Carb. shale	9.62	11	5	604	0.17	1.03	0.49	0.14
	M234	521.35	Shale	0.52	23	50	408	0.03	0.12	0.26	0.23
	M320	299.95	Shale	3.37	14	13	536	0.11	0.49	0.43	0.18

Carb. Shale: carbonaceous shale; TOC: total organic carbon; HI: Hydrogen index; OI: Oxygen index.

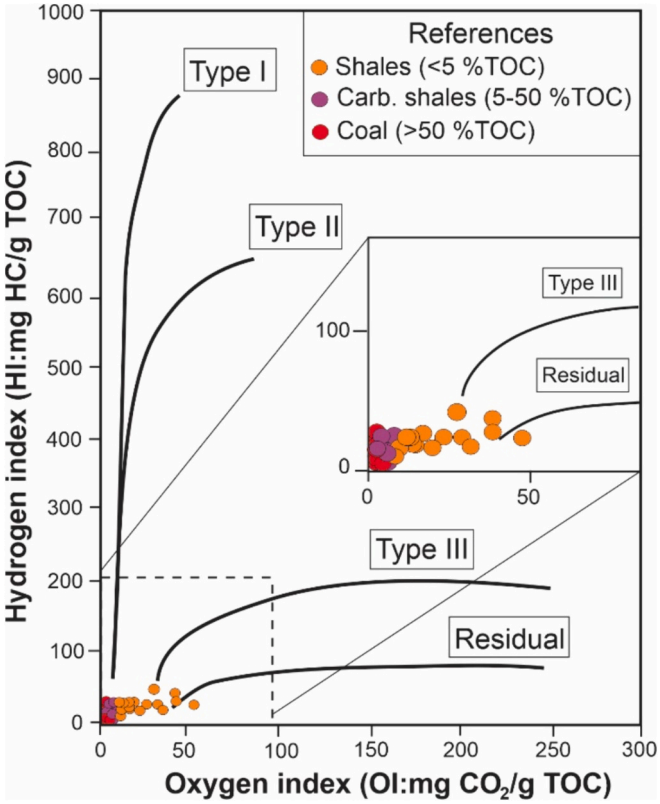

Fig. 4. Hydrogen and Oxygen index data plotted on the pseudo-Van Krevelen diagram, modified from Espitalié et al. (1986). Different colors have been used to indicate different lithologies according to their TOC values.

consist of 10–15 g of rock, selected from the core samples. The rock pieces were ground to a particle size of about 1 mm and blended with a synthetic resin composed of styrene and phthalic anhydride. Rock particles were hardened in resin in a random statistical orientation. The resulting block-rock samples were polished and placed in a silica-gel dryer for a minimum of 24 h prior to microscopic analysis. Samples were analyzed at the University of Geneva (Department of Earth Sciences, Switzerland) using a Zeiss optical microscope under reflected non-polarized white light with an oil immersion objective (50×). The microscope was operated using the DISKUS Fossil software (Hilgers).

Maceral counting was carried out to characterize the organic matter type present in the rock and distinguish vitrinite particles. The identification of organic components was performed according to the ISO-7004-3 (2009) standard. Macerals were identified primarily by their morphology, level of reflectance, and fluorescence intensity under ultraviolet light (Taylor et al., 1998; ICCP, 1998; ICCP, 2001; Suárez-Ruiz et al., 2012). The terminology applied follows the classification and nomenclature of the International Committee for Organic Petrology (ICCP) (ICCP, 1998, 2001; Pickel et al., 2017). Additionally, solid bitumen present in the rock matrix was identified (Suárez-Ruiz et al., 2012).

Vitrinite reflectance (VRo %) measurements were acquired to calibrate the thermal model and asses the maximum thermal conditions attained by the rocks (Welte et al., 1997; Suárez-Ruiz et al., 2012). VRo % data were obtained following the ASTM-D7708–23 (2023) standard for measurements on sedimentary rocks and ISO 7404-5 (2009) for coals. The VRo % values were obtained by measuring between 11 and 77 randomly oriented vitrinite particles on coal and carbonaceous samples and 10 to 80 particles per sample on shales. The number of VRo % measurements was constrained by the low proportion of macerals from the vitrinite group in the organic fraction (mostly <10%; see Section 4.2), and the small size of vitrinite particles (mostly <10 μm), particularly in shales with dispersed organic matter. In the results obtained, the VRo % mean and the lowest and highest VRo % values measured are given. Frequency distribution reflectance histograms and petrologic observations were integrated to differentiate vitrinite populations from semifusinite and/or resedimented particles. The VRo % mean obtained for each sample reflects the most representative measurements of those particles clearly identified as vitrinite.

3.3. Thermal modeling

A 1D (temperature vs time and depth) model was built for the PANG 0001 and PANG 0003 wells to reconstruct the thermal and burial history of the Claromecó Basin sedimentary infill. The model was performed using PetroMod software (Version 2018, Schlumberger). The model was constructed based on the previous geodynamic and tectonic reconstruction of the Claromecó Basin, considering a conceptual geological

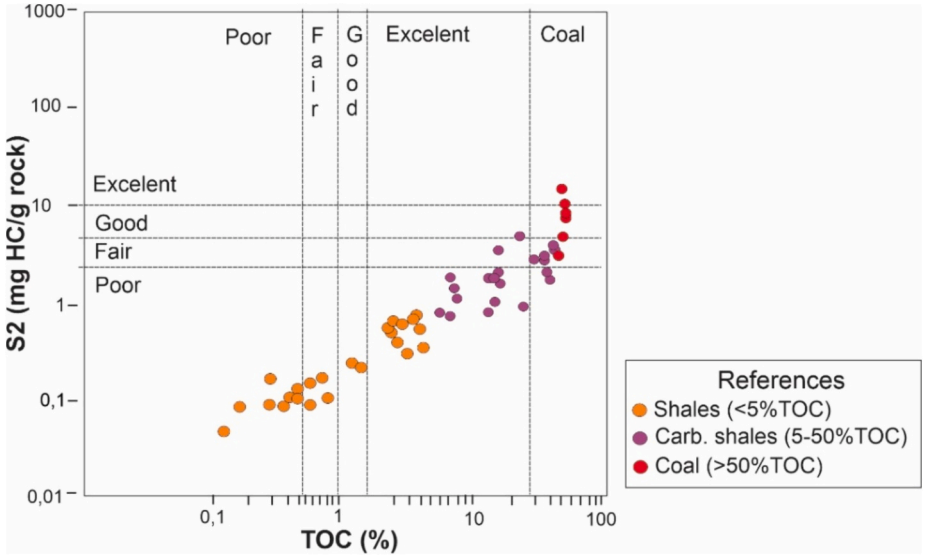

Fig. 5. S2 vs. TOC plot modified from Peters and Cassa (1994). The graphic displays the hydrocarbon potential of the source rock based on the organic carbon content and the amount of hydrocarbon formed during the thermal decomposition of the kerogen (S2). Different colors have been used to indicate different lithologies according to their TOC values.

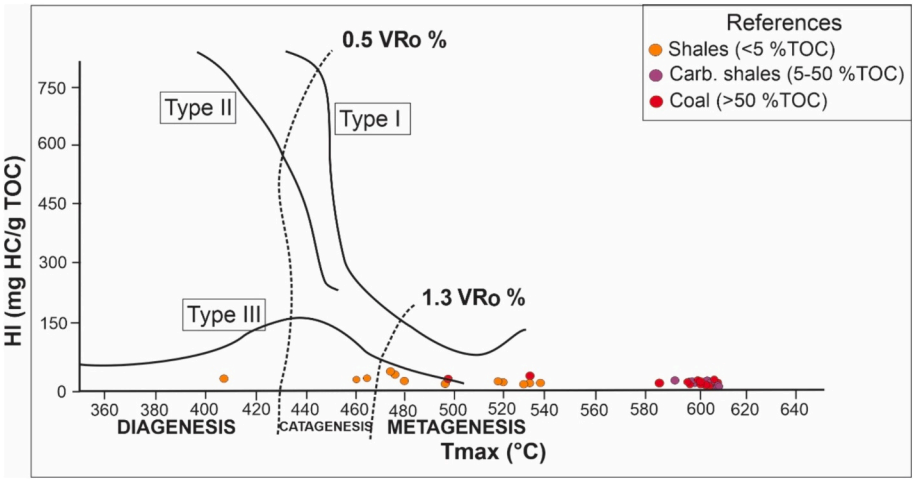

Fig. 6. Hydrogen Index vs. Tmax plot modified from Espitalié et al. (1985b). Most of the samples fall within the wet and condensate gas and dry gas windows. Different colors have been used to indicate different lithologies according to their TOC values.

model that provides the main input data (Table 1; Harrington, 1947, 1970; Suero, 1972; Pángaro and Ramos, 2012; Kollenz et al., 2017; Lovecchio et al., 2018, 2020; Arzadún et al., 2020). The chronological history of the basin was simulated by defining a continuous sequence of depositional, non-depositional, and/or erosional events (Table 1). The Tunas Formation was divided into 5 sub-layers (Tunas 1, Tunas 2, Tunas 3, Tunas 4, Tunas 5) based on the different lithologies that compose this unit (Table 1).

To validate the thermal conditions simulated by thermal modeling, the model was calibrated with VRo % data obtained. Additionally, the thermal model output was corroborated by combining paleothermometric and thermochronometric data from previous works, such as the homogenization temperature of fluid inclusions (Febbo et al., 2023) and apatite fission tracks (AFT; Kollenz et al., 2017; Arzadún et al., 2020). VRo % values were compared with different kinetic curves calculated by the software, including Easy%Ro (Sweeney and Burnham, 1990), Basin %RoDL (Nielsen et al., 2015), and Easy%RoDL (Burnham, 2016). These theoretical curves were calculated by considering the maturation trend as the result of temperature and time, which is a function of the thermal and burial history of the basin. Various scenarios have been tested by changing the variables that most influence the temperature in the basin (basal heat flow and amount of erosion) until the VRo % values fit with the theoretical curves (see Section 4.3). In order to achieve the optimal calibration results, only measurements performed on particles clearly recognized as vitrinite were considered (VRo % mean).

3.3.1. *Boundary conditions – the basal paleo heat flow*

Thermal boundary conditions need to be defined to simulate the temperature reached in the basin infill over time. The upper boundary is the sediment-water interface temperature (SWIT), while the lower boundary condition is the heat flow at the bottom of the basin. Paleotemperature distribution maps are automatically calculated by PetroMod, which defines the evolution of the temperature at sea level by considering variations in global mean surface temperature and latitudinal variation of the study area through time (Wygrala, 1988). The paleo heat flow is critical for the thermal modeling. This parameter is closely related to the geodynamic setting in which the basin forms and evolves, which controls, among other processes, the original lithosphere thickness, the extensional forces, the magmatic activity, and the circulation of deep fluids (Tissot et al., 1987; Allen and Allen, 2005).

Different paleo heat flow scenarios were tested, in which the main variables controlling thermal maturity of the basin infill, basal paleo heat flow and erosion rate, were modified to fit the paleo-thermal data and calibrate the thermal models. The paleo heat flow variation through time was assumed based on the main geodynamic phases of the Claromecó Basin (Fig. 3; Kollenz et al., 2017; Lovecchio et al., 2018; Arzadún et al., 2020). Paleo heat flow values from 60 up to 100 mW/m^2 were assigned during the Early Permian to the Early Cretaceous based on what is proposed in the literature for the different geodynamic settings (Allen and Allen, 2005). The increased heat flow during the Early Permian corresponded to the formation of the foreland basin during the Gondwana Orogeny (MacDonald et al., 2003; Fig. 3). This heat flow trend continued throughout the rifting stage related to lithosphere extension during the breakup of Gondwana supercontinent from Late Triassic to Early Cretaceous (MacDonald et al., 2003; Lovecchio et al., 2018; Fig. 3). During the drift and passive margin periods (Upper Cretaceous–Cenozoic; Fig. 3) the paleo heat flow decreased to values of 60 or even 50 mW/m^2 (Allen and Allen, 2005). Three paleo heat flow scenarios were tested: Scenario 1, with a peak of 80 mW/m^2; Scenario 2, peak of 60 mW/m^2, and Scenario 3, peak of 100 mW/m^2 (Fig. 3).

4. Results

4.1. *Geochemical analyses*

The main parameters obtained in the Rock-Eval analyses are shown in Table 2. Samples analyzed correspond to shales, carbonaceous shales, and coals (Fig. 2). TOC% values vary widely, ranging from 0.13 to 60.35 wt% (Table 2). The higher values correspond to coals (50–60 wt%) and carbonaceous shales (5–50 wt%) and the lower ones to shales (< 5 wt%). The Oxygen index (OI) values are below 50 mg CO_2/g TOC, with the majority of the samples falling within the range of 1 to 8 mg CO_2/g TOC (Table 2; Fig. 4). The Hydrogen index (HI) varies from 3 to 43 mg HC/g TOC, mostly ranging between 10 and 20 mg HC/g TOC (Table 2; Fig. 4). The *HI* vs. *OI* plot (Fig. 4) indicates that Type IV kerogen (residual organic carbon) and, to a lesser extent, Type III kerogen constituted the organic-rich levels. Since the kerogen typing resulting from Rock-Eval data may also be an effect of the thermal maturation process, this result will be confirmed by maceral analysis.

The S1 parameters vary from 0.01 to 0.70 mg HC/g rock. Maximum S1 values were measured in coals and carbonaceous shales, mostly between 0.20 and 0.40 mg HC/g rock (Table 2). The S2 parameters are <11.28 mg HC/g rock and vary according to lithology. S2 values in shales oscillate between 0.04 and 1.59 mg HC/g rock, and in carbonaceous shales and coals from 0.8 to 11.28 mg HC/g rock (Fig. 5). The TOC vs. S2 plot indicates that only coals have good potential as hydrocarbon source rocks (Fig. 5).

The measured Tmax ranges from 408 to 608 °C, increasing with depth (Table 2; Fig. 6). Most of the Tmax values are above 500 °C, falling within the wet and condensate gas and dry gas windows (Fig. 6). Only

Table 3
Results from maceral analysis. Data are mineral matter basis.

Well	Sample	Lithology	Collo. (%)	Vitrod. (%)	Total Vitr. (%)	Fus. (%)	Semif. (%)	Micr. (%)	In. (%)	Macr. (%)	Total Inert. (%)	Sec. (%)	Alg. (%)	Res. (%)	Liptod. (%)	Total Lipt. (%)	Minerals (%)	Bitumen (%)
PANG 0001	**C01**	Carb. shale	3	4	**7**	1	35	–	–	–	**36**	–	1	–	–	**1**	**55**	**1**
	C03	Shale	–	5	**5**	–	20	–	–	–	**20**	–	–	2	–	**2**	**73**	–
	C04	Shale	4	2	**6**	8	40	–	–	–	**48**	–	2	–	–	**2**	**44**	–
	C04A	Carb. shale	4	–	**4**	1	56	4	–	–	**61**	–	2	3	–	**5**	**30**	–
	C05	Shale	3	–	**3**	–	27	–	–	–	**27**	–	–	–	–	–	**70**	–
	C06	Shale	–	10	**10**	–	13	3	–	–	**16**	–	–	–	–	–	**74**	–
	C07	Shale	3	5	**8**	5	22	–	–	–	**27**	–	1	–	–	**1**	**64**	–
	C08	Carb. shale	2	8	**10**	2	26	–	–	–	**28**	–	1	–	–	**1**	**61**	–
	C08A	Carb. shale	6	4	**10**	1	30	1	–	–	**32**	–	3	1	1	**5**	**53**	–
	C09	Carb. shale	10	6	**16**	–	52	–	–	–	**52**	–	–	–	–	–	**32**	–
	C10	Carb. shale	1	1	**2**	1	14	6	–	–	**21**	–	–	–	–	–	**66**	**11**
	C11	Carb. shale	1	1	**2**	–	6	–	–	–	**26**	–	–	–	–	–	**72**	–
	C13	Shale	1	6	**7**	3	32	9	–	–	**44**	–	–	–	–	–	**49**	–
	C14	Shale	–	11	**11**	2	19	1	–	–	**22**	–	–	–	–	–	**67**	–
	C15	Carb. shale	7	1	**8**	24	59	–	–	6	**89**	–	1	2	–	**3**	–	–
	C16	Shale	–	2	**2**	–	15	16	–	–	**31**	–	–	–	–	–	**67**	–
	C17	Shale	1	11	**12**	–	9	5	–	–	**14**	–	–	–	–	–	**74**	–
	C18	Shale	1	11	**12**	–	21	3	–	–	**24**	–	–	–	–	–	**64**	–
	C18 A	Carb. shale	1	1	**2**	1	90	–	–	2	**93**	5	–	–	–	**5**	–	–
	C19	Coal	–	14	**14**	1	7	–	–	–	**68**	–	–	–	–	–	**18**	–
	M6	Shale	1	9	**10**	–	12	5	–	–	**17**	–	–	–	–	–	**73**	–
	M10	Carb. shale	3	5	**8**	12	24	–	–	–	**36**	–	–	–	–	–	**47**	**9**
	M13	Shale	8	4	**12**	1	23	–	–	–	**24**	–	–	–	–	–	**63**	**1**
	M39A	Carb. shale	9	–	**9**	43	48	–	–	–	**91**	–	–	–	–	–	–	–
	M43	Coal	8	–	**8**	9	69	–	–	–	**78**	–	–	–	–	–	**3**	**11**
	M49	Carb. shale	–	1	**1**	2	87	–	–	1	**90**	–	–	1	–	**1**	**8**	–
	M58	Carb. shale	2	7	**9**	4	65	–	–	–	**69**	–	1	1	–	**2**	**19**	**1**
	M61	Shale	–	3	**3**	–	2	–	–	–	**2**	–	–	–	–	–	**95**	–
	M76	Shale	–	3	**3**	–	10	–	–	–	**10**	–	–	–	–	–	**87**	–
	M79	Shale	2	7	**9**	1	24	–	–	–	**25**	–	–	–	–	–	**66**	–
	M80	Carb. shale	18	–	**18**	–	71	–	–	1	**72**	–	1	–	–	**1**	**9**	–
	M80A	Carb. shale	6	–	**6**	5	79	–	–	1	**85**	–	2	–	–	**2**	**7**	–
	M93	Coal	2	–	**2**	2	90	–	–	–	**92**	–	2	–	–	**2**	**2**	**2**
	M95	Carb. shale	2	–	**2**	17	75	–	–	1	**93**	–	–	1		**1**	**2**	**2**
	M97A	Coal	1	2	**3**	5	72	–	–	–	**77**	–	–	1	1	**2**	**18**	–
	M103	Shale	4	1	**5**	1	17	–	–	–	**18**	–	–	–	–	–	**77**	–
PANG 0003	**M110**	Carb. shale	8	3	**11**	6	67	2	1	–	**76**	–	–	–	–	–	**13**	–
	M113	Shale	–	5	**5**	–	23	–	–	–	**23**	–	1	–	–	**1**	**71**	–
	M120	Carb. shale	–	1	**1**	3	43	2	–	–	**48**	–	1	–	–	**1**	**50**	–
	M127	Shale	–	2	**2**	–	4	–	–	–	**4**	–	–	–	–	–	**94**	–
	M139	Carb. shale	1	10	**11**	–	25	–	–	–	**25**	–	–	–	–	–	**64**	–
	M146	Carb. shale	3	6	**9**	–	60	–	–	–	**60**	–	–	–	–	–	**30**	**1**
	M149	Carb. shale	3	6	**9**	–	60	–	–	–	**60**	–	–	–	–	–	**30**	**1**
	M149A	Carb. shale	2	2	**4**	–	73	–	–	–	**73**	–	–	–	–	–	**23**	–
	M153	Carb. shale	2	–	**2**	1	6	–	–	–	**27**	–	–	–	–	–	**71**	–
	M167	Shale	–	6	**6**	–	22	1	–	–	**23**	–	2	–	–	**2**	**69**	–
	M196	Coal	–	2	**2**	–	39	–	–	–	**79**	–	–	–	–	–	**18**	**1**
	M196A	Coal	9	2	**11**	–	89	–	–	–	**89**	–	–	–	–	–	–	–
	M204	Shale	–	1	**1**	–	4	–	–	–	**4**	–	–	–	–	–	**95**	–
	M205	Carb. shale	2	4	**6**	–	49	1	–	–	**50**	–	1	–	–	**1**	**43**	–
	M234	Shale	–	6	**6**	–	20	–	–	–	**20**	–	–	–	–	–	**74**	–
	M242	Shale	–	–	**15**	–	–	–	–	–	**24**	–	–	–	–	–	**61**	–
	M320	Shale	11	8	**19**	–	24	–	–	–	**24**	–	–	–	–	–	**57**	–

Collo.: Collotelinite; Vitrod.: Vitrodetrinite; Total Vitr.: Total Vitrinite group; Fus.: Fusinite; Semif.: Semifusinite; Micr.: Micrinite; In.: Inertinite; Macr.: Macrinite; Total Inert.: Total Inertinite group; Sec.: Secretinite; Alg.: Alginite; Res.: Resinite; Liptod.: Liptodetrinite; Total Lipt.: Total Liptinite group.

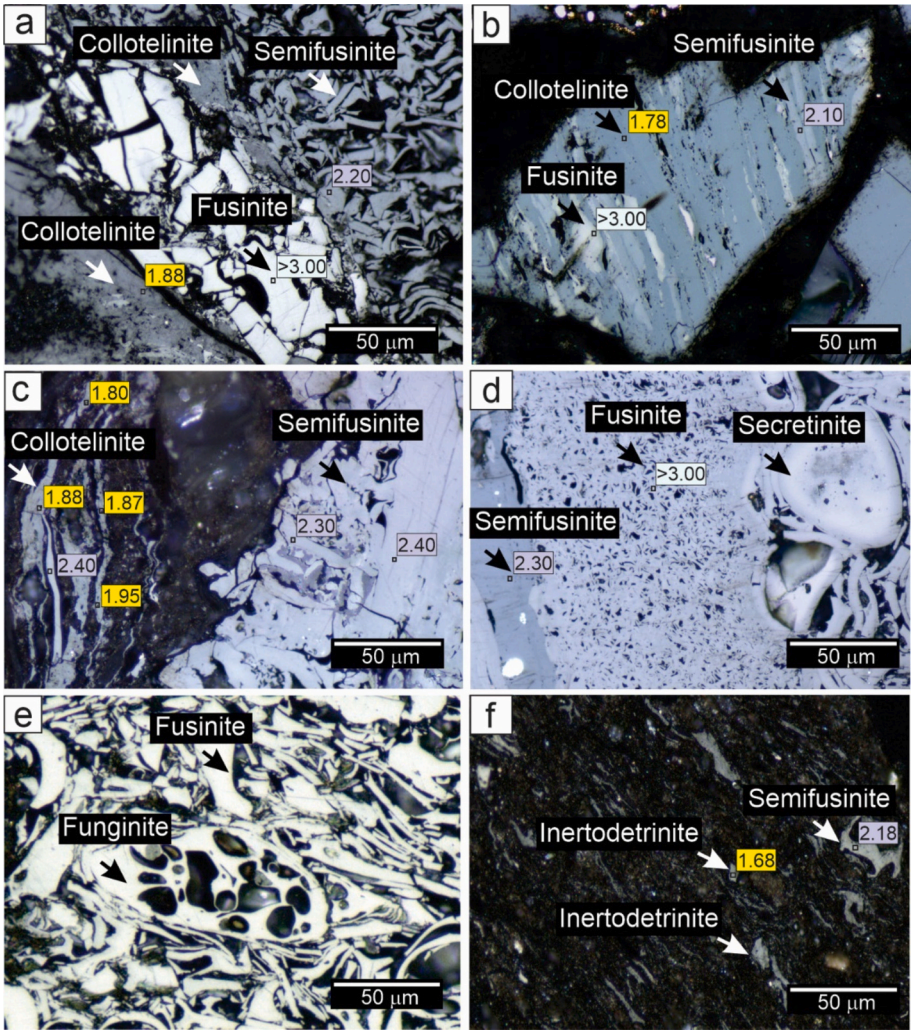

Fig. 7. Photomicrographs of macerals from the inertinite and vitrinite group under reflected non-polarized white light in coals (a-e) and organic-rich shales (f). The values shown in the boxes correspond to the reflectance measurements of each maceral. **a, b, c)** Collotelinite with the lowest reflectance (VRo: 1.78–1.95%), nonvisible vegetal structure, low relief, and grey color; semifusinite with intermediate reflectance (Ro: 2.10–2.40%), preserved plant cellular structure, slight relief, and greyish white; fusinite with high reflectance (Ro: > 3.00%), well-preserved plant cellular structure, high relief, and with color; **d)** Fusinite and secretinite, with high reflectance (Ro: > 3.00%) and well-preserved plant cellular structure, and semifusinite (Ro: 2.30%); **e)** Fusinite and funginite with well-preserved plant cellular structure; **f)** Small particles of inertodetrinite (< 10 µm; VRo: 1.68%) and semifusinite (Ro: 2.18%) dispersed in shales.

three samples, corresponding to shales with low organic matter content (< 0.33 wt%), exhibit Tmax below 490 °C (Fig. 6).

4.2. Organic petrology results

4.2.1. Maceral characterization and analyses

Results from maceral analysis are shown in Table 3. The percentages refer to the bulk rock volume (vol%), including mineral matter content (mineral matter basis). Coals are primarily composed of inertinite (77–92%; Figs. 7a–e) and vitrinite macerals (<10%; Figs. 7a–c), with minor amounts of liptinite macerals (2%; Figs. 8a–e), solid bitumen (1%), and mineral matter (<20%) (Table 3). Carbonaceous shales are characterized by inertinite (20–90%) and vitrinite macerals (< 16%), mineral matter (30–70%, occasionally <20%), and minor proportions of liptinite macerals (< 5%) and solid bitumen (< 10%; Fig. 8f) (Table 3). Shales are dominated by mineral matter (40–95%; Fig. 7f), represented by clays, quartz, and calcite, with minor amounts of dispersed organic matter from the inertinite (15–60%; Fig. 7f) and vitrinite (< 10%; Fig. 7f) groups (Table 3). Framboidal pyrite is common and associated with vitrinite and semifusinite macerals.

Inertinite macerals are largely represented by semifusinite, which is recognized for its preserved plant cell structure, slight relief with respect to the vitrinite particles, and greyish white color (Figs. 7a–d). Semifusinite exhibits an intermediate reflectance between the vitrinite (VRo: < 2.00%; Figs. 7a–c) and the fusinite macerals (Ro: > 3.00%; Figs. 7a, b, d). In minor proportions, small fragments of inertinite macerals (< 10 µm, inertodetrinite; Fig. 7f) and fusinite (Figs. 7a, b, d) were observed. The fusinite exhibits high relief, well-preserved cellular structure, bright white color (Fig. 7a–b, d–e), and high reflectance (Ro: > 3.00%; Figs. 7a, b, d). Macrinite, secretinite (Fig. 7d), and funginite (Fig. 7e) are present in a few samples. Vitrinite macerals are composed of collotelinite, characterized by very low relief, planar morphology, non-visible vegetal structure, and grey color (Figs. 7a–c). Small particles of vitrodetrinite are also present (< 10 µm; Fig. 7f). Vitrinite maceral exhibits lower reflectance than inertinite macerals (Figs. 7a–c). Liptinite macerals are rare and show very faint dark orange fluorescence under UV (Figs. 8a–e). The macerals are mainly represented by resinite (Figs. 8a, b), which fills cells or empty spaces, and liptodetrinite (Fig. 8c, d), formed by small fragments of liptinite (< 10 µm). Alginite and/or sporinite (Figs. 8a,c, d) and suberinite (Fig. 8e) were observed in a few samples. Solid bitumen is rare and is found only in carbonaceous shales, where it fills the space between minerals (Fig. 8f).

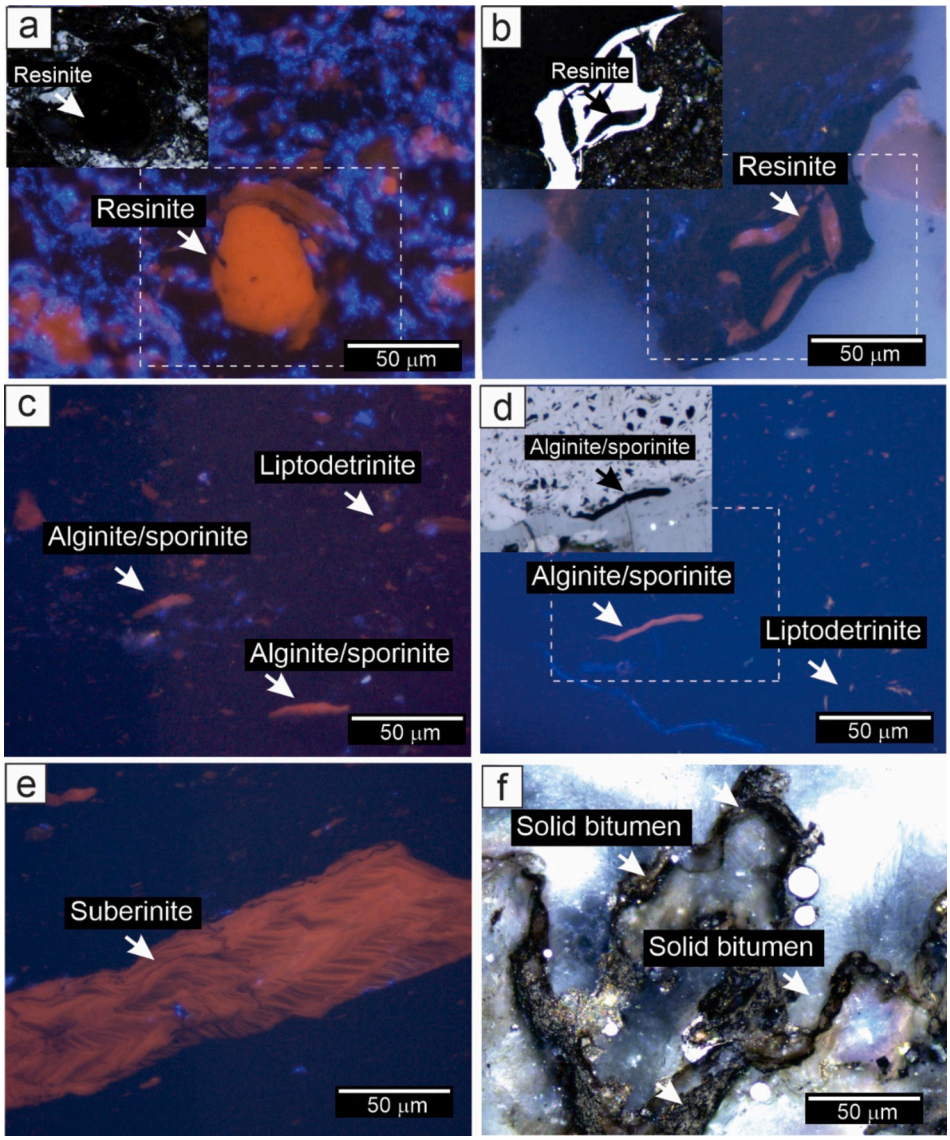

Fig. 8. Photomicrographs of macerals from the liptinite group under fluorescence (a-e) and reflected non-polarized white light (a, b, e – detailed photos) in coals. **a, b)** Resinite filling cavity cells with orange fluorescence under UV and black color under reflected light (detail photo); **c, d)** Small particles of liptodetrinite (< 10 μm) and alginite/sporinite with dark orange fluorescence under UV and black under reflected light (detail photo); **e)** Suberinite with low orange fluorescence under UV; **f)** Solid bitumen filling the space between minerals in carbonaceous shales under non-polarized white light. (For interpretation of the references to color in this figure legend, the reader is referred to the web version of this article.)

Petrologic observations confirm the predominance of residual organic matter (Type IV kerogen, represented by the inertinite group and solid bitumen) and to a lesser extent presence of terrestrial organic matter (Type III kerogen, represented by the vitrinite group) in the analyzed samples. These results are consistent with the geochemical data (Fig. 4).

4.2.2. Vitrinite reflectance measurements

Reflectance ranges for vitrinite were stated for each sample by taking between around 100 reflectance measurements where possible, with between 10 and 80 measurements taken on clearly recognizable vitrinite particles (Table 4). Reflectance measurements of vitrinite, semifusinite, and resediment particles show a wide range, from 1.35 to 2.80%. The large variation in measurements is due to the difficulty in distinguishing between vitrinite and semifusinite (inertinite) particles. Vitrinite particles were identified by their morphology (non-preserved cellular structure, planar morphology, and very low relief; Fig. 7 a-c). These particles have a lower reflectance (VRo: < 2%) compared to particles distinguished by their morphology as semifusinite macerals and/or resedimented vitrinite particles (Ro: > 2%) (e.g., Figs. 7a-c, f). The number of VRo % measurements was constrained by the low proportion of vitrinite macerals in the organic fraction (< 10%; see Section 4.2) and the small size of vitrinite particles (mostly <10 μm), particularly in shales with dispersed organic matter, which made measurements dismissible due to surface inhomogeneity and inadequate particle identification.

Two populations were interpreted in each sample based on petrologic observations and frequency distribution histograms (Fig. 9). The lower reflectance values measured (VRo: 1.45–2.00%; Fig. 9, yellow area) were assigned to proper vitrinite particles and used to estimate the VRo % mean (Table 4). The highest reflectance values (Ro: 2.00–2.80%; Fig. 9, blue area) are attributed to semifusinite and/or resedimented particles and were therefore excluded from the VRo % mean estimation. The latter group is better represented in the reflectance histograms as the samples are mainly composed of semifusinite macerals (Figs. 4, 9; Table 3). For the population interpreted as vitrinite, the VRo % mean as

Table 4
Vitrinite reflectance measurements results.

Well	Sample	Depth	Lithology	Low. reflect.	High. reflect.	Low. VRo %	High. VRo %	VRo % mean	SD	N° vitrinite	N° total
PANG 0001	C01	863.19	Carb. shale	1.45	2.45	1.45	2.00	**1.90**	0.26	70	100
	C03	858	Shale	1.35	2.33	1.35	2.00	**1.95**	0.17	60	74
	C04	856.87	Shale	1.40	2.20	1.40	1.93	**1.90**	0.14	66	70
	C04A	855.5	Carb. shale	1.45	2.70	1.45	1.90	**1.90**	0.13	35	75
	C05	853.5	Shale	1.35	2.65	1.35	1.98	**1.95**	0.20	22	42
	C06	850	Shale	1.49	2.55	1.49	2.03	**1.85**	0.15	23	54
	C07	847.5	Shale	1.46	2.45	1.46	1.95	**1.85**	0.14	76	100
	C08	813.4	Carb. shale	1.60	2.50	1.60	2.00	**1.87**	0.09	12	100
	C08A	812	Carb. shale	1.65	2.63	1.65	2.00	**1.90**	0.18	35	100
	C09	810.6	Carb. shale	1.80	2.44	1.80	2.00	**1.90**	0.04	36	100
	C10	801.8	Carb. shale	1.77	2.40	1.77	2.00	**1.90**	0.04	22	100
	C11	790.6	Carb. shale	1.79	2.46	1.79	2.00	**1.85**	0.07	20	100
	C13	709.35	Shale	1.40	2.50	1.40	1.95	**1.80**	0.12	42	100
	C14	420.8	Shale	1.30	2.50	1.30	1.70	**1.50**	0.12	37	100
	C15	418.6	Carb. shale	1.65	2.38	1.65	1.90	**1.65**	0.08	46	100
	C16	358.82	Shale	1.60	2.60	1.60	1.75	**1.60**	0.05	19	100
	C17	358.44	Shale	1.35	2.50	1.35	1.88	**1.60**	0.14	43	100
	C18	355	Shale	1.35	2.35	1.45	1.80	**1.50**	0.14	62	98
	C18 A	355.5	Carb. shale	1.35	2.45	1.35	1.80	**1.50**	0.11	33	91
	C19	354.7	Coal	1.36	1.88	1.36	1.75	**1.45**	0.14	77	100
	M6	896.3	Shale	1.48	2.80	1.48	2.00	**2.00**	0.16	38	100
	M10	893.05	Carb. shale	1.77	2.51	1.77	2.10	**2.00**	0.07	12	100
	M13	888.4	Shale	1.45	2.39	1.45	2.00	**1.90**	0.16	80	96
	M39A	853.28	Carb. shale	1.70	2.38	1.70	2.00	**1.95**	0.09	30	100
	M43	850.54	Coal	1.66	2.57	1.66	2.00	**1.95**	0.10	35	100
	M49	842.4	Carb. shale	1.70	3.00	1.70	2.00	**1.90**	0.11	22	100
	M58	832.3	Carb. shale	1.50	2.70	1.50	2.00	**1.87**	0.11	50	100
	M61	829.47	Shale	1.45	2.65	1.45	2.00	**1.90**	0.15	33	100
	M76	810.34	Shale	1.38	2.70	1.38	2.00	**1.90**	0.16	58	91
	M79	809.03	Shale	1.42	2.80	1.42	2.00	**1.90**	0.16	37	100
	M80	807	Carb. shale	1.88	2.57	1.88	2.10	**1.90**	0.04	15	100
	M80A	807.75	Carb. shale	1.83	2.56	1.83	2.10	**1.95**	0.06	25	100
	M93	798	Coal	1.87	2.84	1.87	2.20	**1.90**	0.06	25	100
	M95	797.15	Carb. shale	1.62	2.65	1.62	1.95	**1.90**	0.10	11	100
	M97A	786.25	Coal	1.52	2.80	1.52	2.00	**1.90**	0.14	30	100
	M103	778.53	Shale	1.80	2.76	1.80	2.00	**1.90**	0.07	10	100
PANG 0003	M110	770.5	Carb. shale	1.77	2.69	1.70	2.00	**1.85**	0.07	20	100
	M113	768.14	Shale	1.60	2.80	1.60	1.95	**1.85**	0.10	30	100
	M120	752.77	Carb. shale	1.30	2.60	1.30	1.90	**1.80**	0.13	43	61
	M127	743.86	Shale	1.75	2.45	1.75	2.00	**1.85**	0.07	21	50
	M139	729.56	Carb. shale	1.48	2.60	1.50	1.90	**1.80**	0.14	51	100
	M146	720.31	Carb. shale	1.78	2.68	1.78	2.00	**1.80**	0.08	23	100
	M149	714.53	Carb. shale	1.55	2.66	1.55	1.95	**1.75**	0.08	32	100
	M149A	715	Carb. shale	1.54	2.90	1.54	1.98	**1.85**	0.12	15	100
	M153	707.3	Carb. shale	1.69	2.63	1.69	1.90	**1.80**	0.07	18	100
	M167	693.08	Shale	1.65	2.60	1.60	1.95	**1.80**	0.07	53	88
	M196	634.2	Coal	1.50	2.49	1.50	1.90	**1.80**	0.11	25	100
	M196A	635	Coal	1.67	2.80	1.67	1.95	**1.80**	0.08	50	100
	M204	619	Shale	1.65	2.60	1.65	1.90	**1.70**	0.10	18	45
	M205	618	Carb. shale	1.57	2.65	1.57	1.90	**1.75**	0.11	18	100
	M234	531.35	Shale	1.55	2.80	1.55	1.85	**1.60**	0.06	15	100
	M242	521.25	Shale	1.50	2.65	1.50	1.80	**1.60**	0.11	27	100
	M320	299.95	Shale	1.35	2.32	1.35	1.80	1.50	0.10	72	100

Low./High. reflect.: lowest/highest values of the total reflectance measurements (include vitrinite + semifusinite/resedimented particles); Low./High. VRo %: lowest/highest values of the vitrinite reflectance measurements; VRo % mean: most representative vitrinite reflectance values of clearly recognizable vitrinite particles; SD: standard deviation; N° vitrinite: Number of vitrinite particles measured; N° part.: Number of total particles measured.

well as the range of measured values (lowest and highest VRo % value) were stated for each sample (Table 4). The VRo % mean obtained for each sample reflects the most representative measurements of those particles clearly identified as vitrinite.

4.3. Thermal model calibration

In order to validate the thermal conditions simulated by thermal modeling, the models were calibrated with the vitrinite reflectance data previously obtained (VRo % mean; Table 4). Calibration was performed using only the VRo % measurements obtained in those particles properly recognized as vitrinite (Fig. 9, yellow area). Three different kinetic curves (Easy%Ro, Sweeney and Burnham, 1990; Basin%RoDL, Nielsen et al., 2015; Easy%RoDL, Burnham, 2016) were tested and calibrated with the VRo % mean values (Fig. 10; Table 4). The Easy%Ro curve (Sweeney and Burnham, 1990) provides the best fit to the measured paleothermal data (Fig. 10). The kinetic curve Easy%Ro DL (Burnham, 2016) only fits with the VRo % mean data from the upper levels (Tunas 4 and 5), while the kinetic simulation Basin%Ro DL (Nielsen et al., 2015) cannot fit the VRo % values from shallower layers (Tunas 1, Fig. 10). Therefore, the Easy%Ro kinetic curve was used to test different scenarios and reconstruct the thermal history of the basin.

To calibrate the VRo % data, three scenarios were tested by combining different trends of paleo heat flow over time (Fig. 3) and erosion magnitudes (Fig. 11, Table 5). The heat flow trend scenario 1 (80 mW/m^2) showed the best fit with the VRo % measured at erosion thicknesses of 3000 m (Fig. 11a, Table 5). Erosion values below 2700 m could only be fitted with the minimum values of VRo %, while erosion

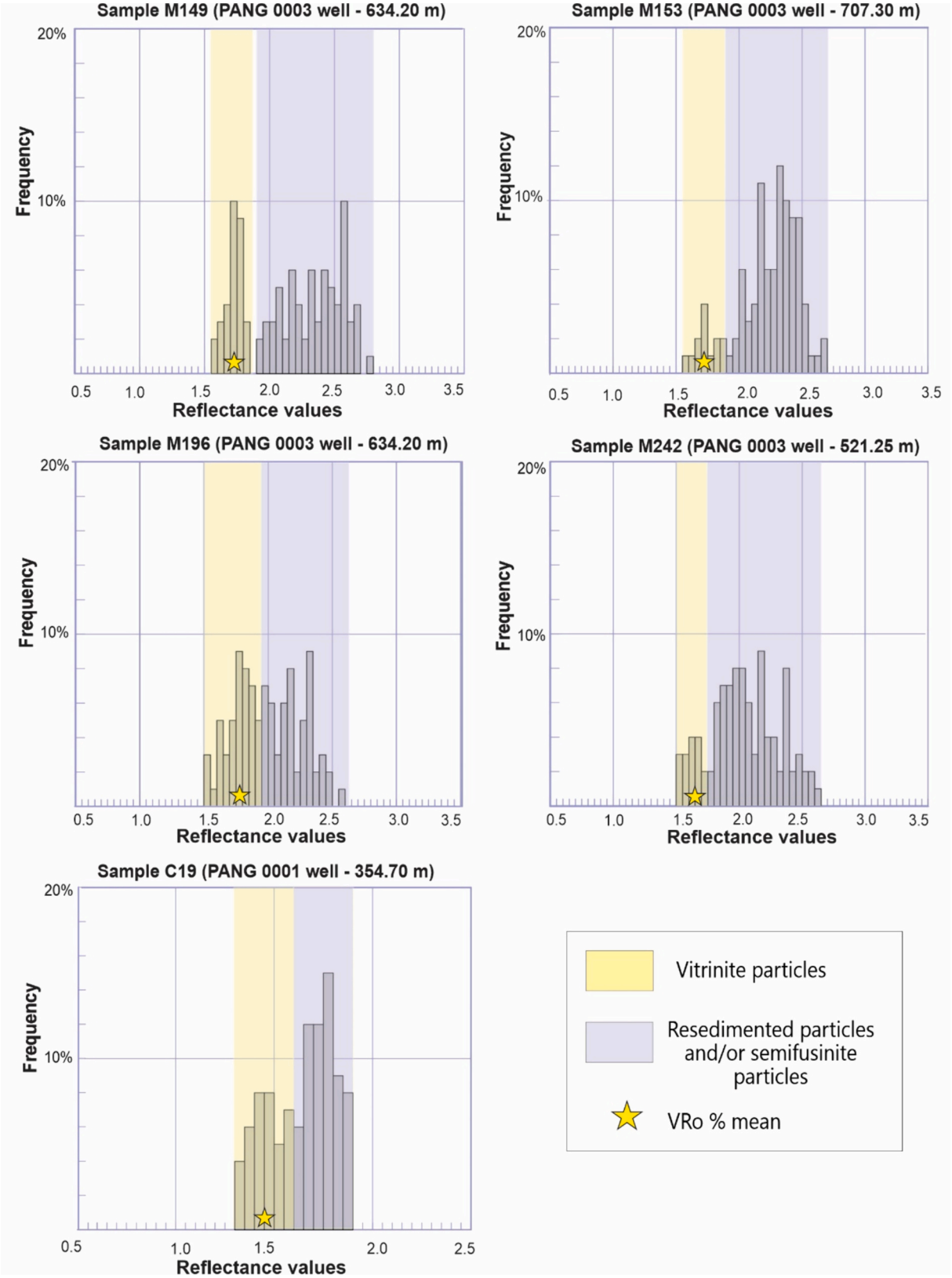

Fig. 9. Reflectance frequency histograms with the 2 populations interpreted (vitrinite particles, yellow area, and semifusinite and/or resedimented particles, blue area) and %VRo mean (yellow star), which reflects the most representative vitrinite reflectance values of clearly recognizable vitrinite particles. (For interpretation of the references to color in this figure legend, the reader is referred to the web version of this article.)

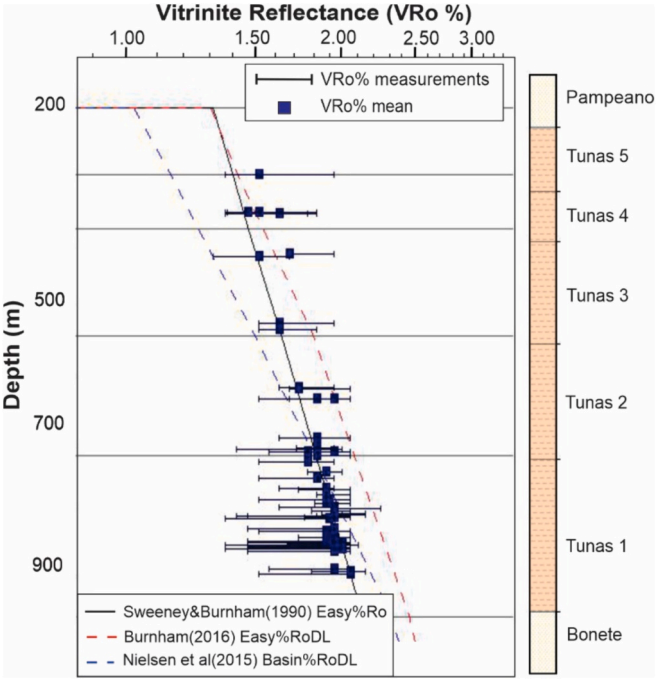

Fig. 10. Calibration of the thermal model for the Tunas Formation (PANG 0001 and PANG 0003 wells) with VRo % total measurements (based on lowest and highest VRo % values, indicated by the blue lines) and VRo % mean, considering different kinetic curves. (For interpretation of the references to color in this figure legend, the reader is referred to the web version of this article.)

thicknesses above 3200 m were only calibrated with VRo % values of the shallow stratigraphic levels (Tunas 4 and 5; Fig. 11a, Table 5). In the paleo heat flow scenario 2 (60 mW/m^2), a cooler heat flow trend is assumed compared to scenario 1. Therefore, a larger amount of erosion is needed to calibrate the paleothermal data (Fig. 11b, Table 5). In this case, the best fit with the VRo % results (Fig. 11b, Table 5) were achieved with erosion thicknesses of 4200 m (Fig. 11b, Table 5). Erosion amounts of 4000 m could only be adjusted with the minimum VRo % data (Fig. 11b, Table 5), whereas erosion thicknesses of 4400 m were only calibrated with %Ro values of the shallowest stratigraphic levels (Tunas 4 and 5; Fig. 11b, Table 5). Finally, scenario 3 considers the highest heat flow trend (100 mW/m2), thus, a lower amount of erosion (<2500 m) is required to calibrate the model. However, this scenario does not provide a satisfactory calibration when considering the total VRo % obtained (Fig. 11c, Table 5). For an erosion magnitude of 2100 m, only the VRo % data measured in the lower stratigraphic level (Tunas 1) showed a good calibration (Fig. 11c, Table 5), while erosion magnitudes above 2300 m matched only with VRo % values from the shallower stratigraphic levels (Tunas 4 and 5; Fig. 11c, Table 5). Based on the tested variables and their resulting calibration, two thermal models, Model A and Model B, were constructed (Fig. 12; Table 5).

4.4. Thermal modeling outputs

The modeling output from the Model A and Model B are shown in Fig. 12. Model A was based on the variables tested in scenario 1 (paleo heat flow of 80 mW/m^2 and erosion of 3000 m; Table 5), while Model B was based on the variables tested in Scenario 2 (paleo heat flow of 60 mW/m^2 and erosion of 4200 m; Table 5). Both models show similar temperature trends (Figs. 12a, b). The maximum paleotemperatures reached by the Tunas Formation were 183 °C for Model A (Scenario 1; Fig. 12c) and 181 °C for Model B (Scenario 2; Fig. 12d). These temperatures were attained during the Upper Triassic, between 209 Ma (Model A, Fig. 12c) and 202 Ma (Model B; Fig. 12c). In particular, the upper organic-rich level reached maximum temperatures of 160 °C (Tunas 4; Fig. 12c, d) and the lower levels of 180 °C (Tunas 1; Figs. 12c, d).

5. Discussions

5.1. Thermal and burial history of the Claromecó foreland Basin

The basal paleo heat flow trend over time and the maximum burial, defined by the thickness of the stratigraphic record plus the thickness removed by erosion, are the main factors influencing the thermal history of the basin infill. The different models tested show that paleo heat flow trends with maximum peaks in the range of 60–80 mW/m^2 provide the best calibration results (Table 5). Under these thermal conditions, an accumulation and subsequent exhumation and erosion thicknesses of 3000 m (Scenario 1, Model A; Figs. 11a, 12a) or 4200 m (Scenario 2; Model B, Figs. 11b, 12b) were required to validate the VRo % data. The heat flow scenario 1 (Model A; Fig. 12a) seems to be the most appropriate for reconstructing the thermal history of the basin since similar heat flow values have been proposed in the literature for collisional belts and foreland areas (Allen and Allen, 2005). Based on the thermal model reconstruction, the maximum paleotemperature for the Tunas Formation is estimated to be approximately 180 °C (Fig. 12).

To corroborate the thermal modeling results, paleothermal data obtained in previous works, such as fluid inclusions (FI) and apatite fission tracks (AFT) were implemented (Fig. 12). Homogenization temperatures (Th) obtained in fluid inclusions have an average of 160 °C (±20) for carbonate cement and 180 °C (±20) for calcite and quartz veins (Febbo et al., 2023; Figs. 12a, b). In the reconstructed thermal models, the maximum paleotemperatures reached by the Tunas Formation (181–183 °C; Figs. 12c, d) are consistent with the paleotemperatures obtained from fluid inclusion measurements. Apatite fission track data obtained on samples from PANG 0003 well indicate a late Early Cretaceous cooling event (Barremian–Aptian, 125.8 ± 10.6 Ma; Arzadún et al., 2020) when the unit reached temperatures of approximately 90–100 °C (Figs. 12a, b). Additionally, Kollenz et al. (2017) report AFT ages ranging from 120.8 ± 7.3 to 107.4 ± 3.5 Ma for samples belonging to outcrops of the Tunas Formation. These results indicate a cooling event during the Cretaceous, consistent with subsurface data. According to the models simulated, paleotemperatures reached by the Tunas Formation in the Lower Cretaceous are between 95 and 100 °C, fitting with the AFT data from both scenarios (Figs. 12a, b).

5.2. Insights on the geodynamic evolution of the Claromecó Basin

The thermal modeling results obtained in this work provide essential data for a better understanding of the subsidence and erosion processes in the Claromecó Basin, and thus of the geodynamic evolution of the area. The deposition and rapid burial of the Tunas Formation sediments occurred in the foreland basin stage, during the Lower Permian to early Late Triassic periods (Fig. 12). According to the reconstructed models, at least 3000 m of sediments were accumulated during this phase, reaching maximum burial depth of 3000 m (Model A; Fig. 12a) and 4000 m (Model B; Fig. 12b) in the Late Triassic (~ 209 Ma), 50 Ma after deposition. The magnitude of the accumulated thicknesses could be explained by rapid subsidence during the formation of the foreland basin in response to a lithospheric flexural loading mechanism that occurred during the deformation and uplift of the Sierras Australes fold and thrust belt (Gondwanides Orogeny phase; De Wit et al., 1988; Williams, 1995; Milani and De Wit, 2008). Indeed, this period of accelerated subsidence is well documented in other southwestern Gondwana basins (e.g., Paraná and Karoo basins), where an accumulation from 1.5 to 3 km of sediment was recorded during the Late Permian–Triassic (Fernandes et al., 2015; Bicca et al., 2020).

During the Mesozoic, rifting events affected the SW margin of Gondwana, leading to the formation of the Colorado and Salado basins (Mpodozis and Ramos, 2008; Lovecchio et al., 2018) and the opening of

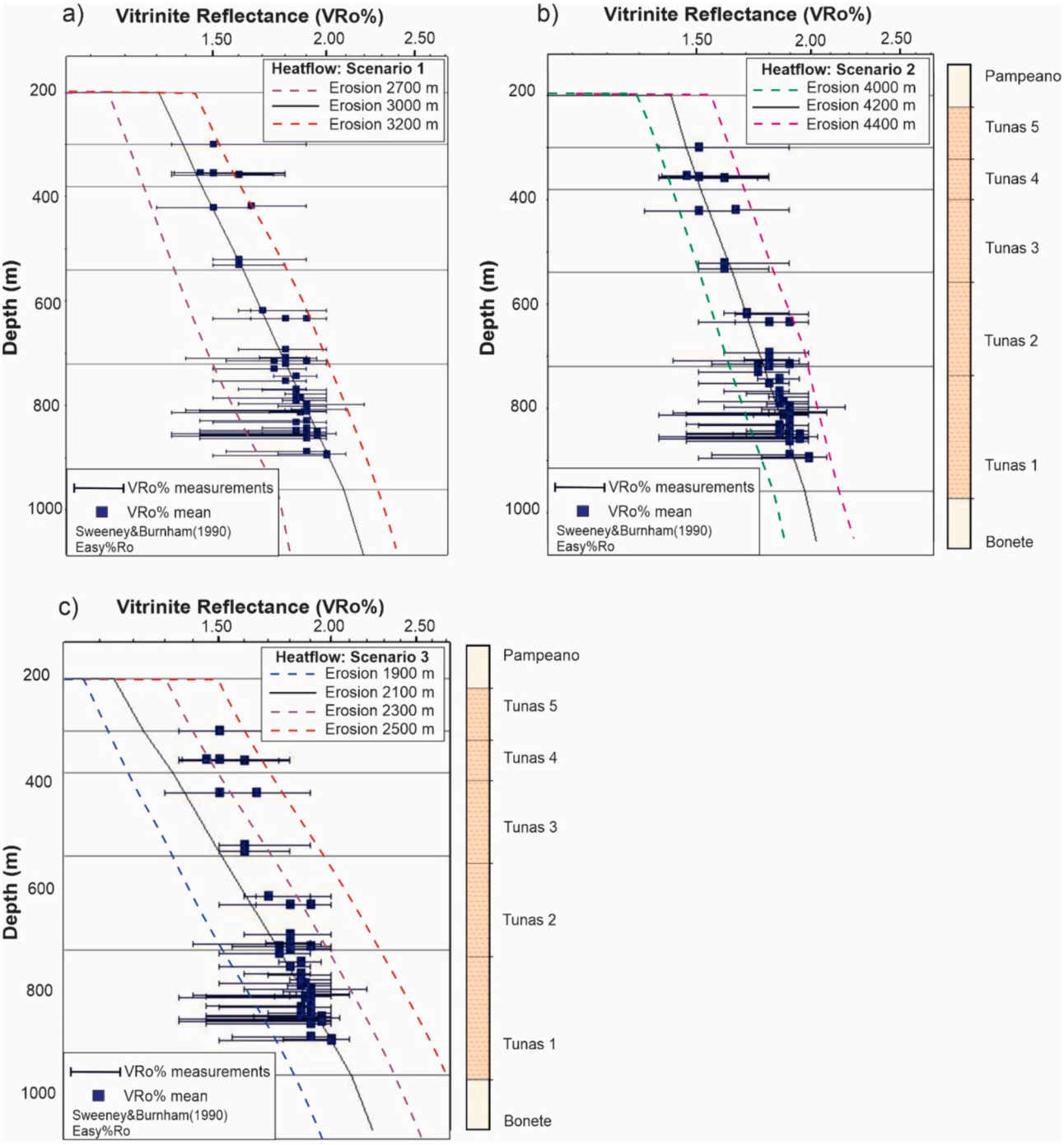

Fig. 11. Calibration of thermal modeling for the Tunas Formation in the PANG 0001 and PANG 0003 wells considering different paleo heat flow and erosion scenarios. The graphics show the VRo % vs. depth plot, the theoretical Easy %Ro curve applying the Sweeney and Burnham (1990) kinetic and its changes due to erosion rates, and the VRo % measurements. Calibration was performed with the VRo % mean values.

the South Atlantic Ocean (Larson and Ladd, 1973; Heine et al., 2013). Towards the initial and *syn*-rift stages (Late Triassic–Jurassic) (Fig. 3), the Claromecó Basin experienced uplift and erosion of at least 1000–2000 m of the stratigraphic record, according to the models proposed in this work (Figs. 12a, b). This exhumation was interpreted as a rift flank exhumation since this area acted as the northern shoulder of the Colorado Basin (Arzadún et al., 2020). The rifting period is followed by a post-rift phase during which the study area evolved as a passive margin (Fig. 3; Kollenz et al., 2017). Significant uplift episodes could have affected the basin during the transition from the rifting to the drift stage (Early Cretaceous–Cenozoic), resulting in the erosion of another 2000 m of sediments (Figs. 12a, b). The exhumation of passive margins during the transition from rifting to drifting has been documented in other basins and is known as the breakup/post-rift unconformity (Withjack et al., 2020 and references therein). In the case of the Claromecó Basin, the Permian-Cenozoic unconformity recorded could be explained by this uplift mechanism.

In summary, the uplift and exhumation of at least 3000 m of sediments affected the infill of the Claromecó Basin from the Late Triassic to the Cenozoic. The proposed erosion values are consistent with those estimated by other authors, which range from 2000 to 3000 m of sediments, based on AFT data (Kollenz et al., 2017; Arzadún et al., 2020),

Table 5
Scenarios tested for thermal model calibration where different paleo heat flow trends and erosion magnitudes are proposed.

Paleo heat Flow trend	Paleo heat Flow value (mW/m^2)	Permian-Cenozoic erosion (m)	Calibration results	Model output
Scenario 1	80	2700	Not calibrated	**Model A**
		3000	**Calibrated**	
		3200	Not calibrated	
Scenario 2	60	4000	Not calibrated	**Model B**
		4200	**Calibrated**	
		4400	Not calibrated	
Scenario 3	100	1900	Not calibrated	–
		2100	Not calibrated	
		2300	Not calibrated	
		2500	Not calibrated	

seismic interpretation and subsidence curves (Pángaro and Ramos, 2012; Pángaro et al., 2015).

5.3. Hydrocarbon potential of the Tunas Formation coal deposits

The potential of source rocks to generate significant amounts of hydrocarbons is commonly assessed in terms of i) the amount of organic matter in the rock; ii) the quality and type of organic matter capable of producing hydrocarbons; and iii) the maturity of the organic matter (Tissot and Welte, 1984; Magoon and Dow, 1994). In this paper, the hydrocarbon potential of the coal-bearing deposits of the Tunas Formation has been estimated based on geochemical and petrologic data and thermal modeling results. Rock-Eval pyrolysis results show TOC% values ranging from 0.13 to 60.35 wt%, with an average of 3.32% in shales, 28.86% in carbonaceous shales, and 56.97% in coals (Table 2). Along with TOC, S2 (hydrocarbon potential index) values were used values to determine the current potential of the source rocks to generate and release hydrocarbons (Peters and Cassa, 1994). Results indicate a current low to non-potential for shales (< 2 mg HC/g rock), low to fair potential to carbonaceous shales (2–4 mg HC/g rock), and mostly good potential for coals (2–11 mg HC/g rock) based in the ranges suggested by Peters and Cassa (1994) (Fig. 5, Table 2). Identifying different types of kerogen is useful for evaluating source rocks and determining which hydrocarbons may form during thermal maturation. The Hydrogen (< 50 mg HC/g TOC; Table 2) and Oxygen (< 50 mg CO_2/g TOC; Table 2) indexes obtained from pyrolysis indicate the dominance of Type IV residual kerogen and a minor amount of Type III terrestrial kerogen (Fig. 4). The residual kerogen could be the result of the thermal maturation of an original Type III kerogen. Petrologic observations confirm that the organic matter contained in the analyzed samples is mainly composed of inertinite macerals, as well as minor amounts of vitrinite and liptinite. Most of the samples display a Tmax ranging from 460 to 610 °C, indicating a late catagenesis to metagenesis stage within the wet to dry gas window (Espitalié et al., 1985b; Table 2, Fig. 6). Further, low values of HI (< 20 mg HC/g TOC) and Tmax above 500 °C confirm a post-mature stage within the dry gas window for coal deposits (Mukhopadhyay et al., 1995). This stage of thermal maturity is corroborated by VRo % data, which mostly range between 1.50 and 2.00%, indicating a wet to dry gas window (Fig. 13). Geochemical data and VRo % results are validated by paleothermal indicators such as fluid inclusions and mineral associations (Febbo et al., 2023), which confirm that the Tunas Formation reached a late catagenesis to metagenesis stage, with paleotemperatures between 150 and 200 °C.

Thermal modeling provides the evolution of the thermal maturity of the entire stratigraphic section of the Claromecó Basin over time in a burial vs. time plot (Fig. 13). Results from the thermal Model A are shown as an example (Fig. 13), as similar results are obtained also for the Model B. The present-day thermal maturity of the Tunas Formation (gas window) was attained when the basin infill reached its maximum burial depth, in the Late Triassic, when about 3000 m of sediments were deposited.

In conclusion, coal beds of the Tunas Formation could have a current potential as gas-prone source rocks upon reaching thermal maturation. At present, the hydrocarbon generation capacity of coal levels is low (S2 < 11 mg HC/g rock, HI < 50 mg HC/g TOC) due to the high percentage of residual kerogen (Type IV) that constitutes the organic fraction. However, since the studied stratigraphic section reached the oil to gas window thermal conditions relatively early in its burial history (Permian-Triassic time), the potentially expelled hydrocarbons could have been lost due to migration or could be trapped somewhere in the basin if the traps were already present in this early evolution phase of the basin. To improve the understanding of the hydrocarbon potential of the area, further studies are needed that take into account the geometry (2D section or 3D model) and the structural evolution of the basin.

5.4. Uncertainties of the model results

The results of the thermal modeling improve the understanding of the geodynamic evolution of southwestern Gondwana during the Late Paleozoic–Mesozoic and provide important insights for the exploration of energy resources in Argentina. However, due to the various assumptions made in the construction of the thermal models, several key uncertainties in the results must be accepted. The most uncertain variables controlling the volume estimates are listed below.

- Vitrinite reflectance data used to calibrate the model: The VRo % values used to calibrate the thermal models display a high dispersion as reflected by a large standard deviation (SD > 1.0%). Uncertainties may be related to the difficulty of distinguishing between the vitrinite and semifusinite particles. To improve the reliability of our interpretation, additional samples, representative also of uppermost and lowermost stratigraphic layers, must be analyzed, to better identify the VRo % trend with depth. Studying samples from nearby wells would also help to improve the understanding of the thermal maturity trend of the basin.
- The paleo heat flow: The paleo heat flow variation with time and the different scenarios tested in this work are based on those proposed in the literature for different geodynamic settings (Allen and Allen, 2005). A proper estimation of the paleo heat flow in the Claromecó Basin could be obtained by subsidence analysis and lithosphere models (e.g., Royden, 1986), which are beyond the scope of this work.
- The geodynamic evolution of the area: The tectonic and stratigraphic evolution of the Claromecó Basin is poorly constrained to date due to the lack of Paleozoic outcrops in the foreland area and the scattered and scarce subsurface data available. Therefore, the timing of the deposition and erosion of the missing Mesozoic section is uncertain. In order to reconstruct the thermal models, we used literature data (IF and AFT) obtained in Tunas Formation outcrops and cores as main constraints (Kollenz et al., 2017; Arzadún et al., 2020; Febbo et al., 2023). In the future, the results of this work can be improved by the acquisition of new paleotemperature and geochronological data, which can date the main burial and uplift events.
- Source rock lateral facies variation: The organic-rich facies can vary along the basin depending on the depositional paleoenvironment. The proximity of the depositional sink with regards to the palaeocontinent controls the composition of the coal-bearing deposits (kerogen amount and maceral composition). Therefore, the hydrocarbon potential of the Tunas Formation in other points of the basin

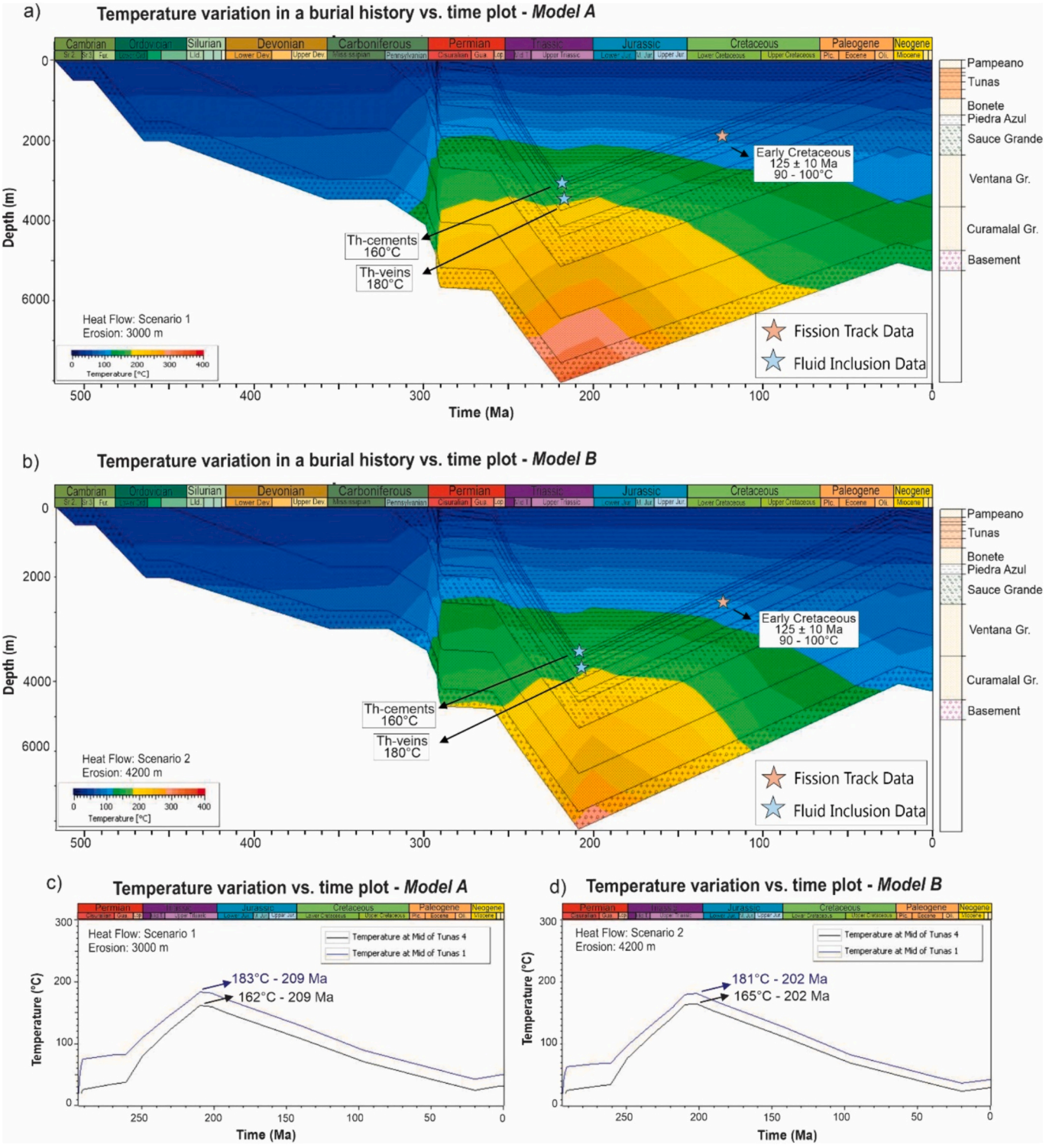

Fig. 12. a, b) Burial vs. time plot for the Tunas Formation (PANG 0001 and PANG 0003 wells) showing the temperature variation over time considering: **a)** paleo heat flow Scenario 1 (80 mW/m^2) and erosion of 3000 m for Model A; **b)** paleo heat flow Scenario 2 (60 mW/m^2) and erosion of 4200 m for Model B. The models were validated with homogenization temperature (Th) obtained in fluid inclusions (Febbo et al., 2023) and apatite fission tracks data (Kollenz et al., 2017; Arzadún et al., 2020); **c, d)** Temperature vs. time plot showing the maximum temperatures achieved by the Tunas Formation upper (Tunas 1) and lower (Tunas 4) coal-bearing levels, considering: **c)** the paleo heat flow Scenario 1 (80 mW/m^2) and erosion thicknesses of 3000 m for Model A; **d)** the paleo heat flow Scenario 2 (60 mW/m^2) and erosion thicknesses of 4200 m for Model B.

may be different from that estimated in the wells analyzed in this work. The accessibility to other subsurface samples would improve the knowledge of the facies distribution and depositional environments variation of the Tunas Formation throughout the basin.

- Hydrocarbon potential of the Claromecó Basin: The realization of a 2D thermal model, based on a geological cross-section of the basin can improve the assessment of a potential petroleum system in the Claromecó Basin. A 2D model takes into account the stratigraphic

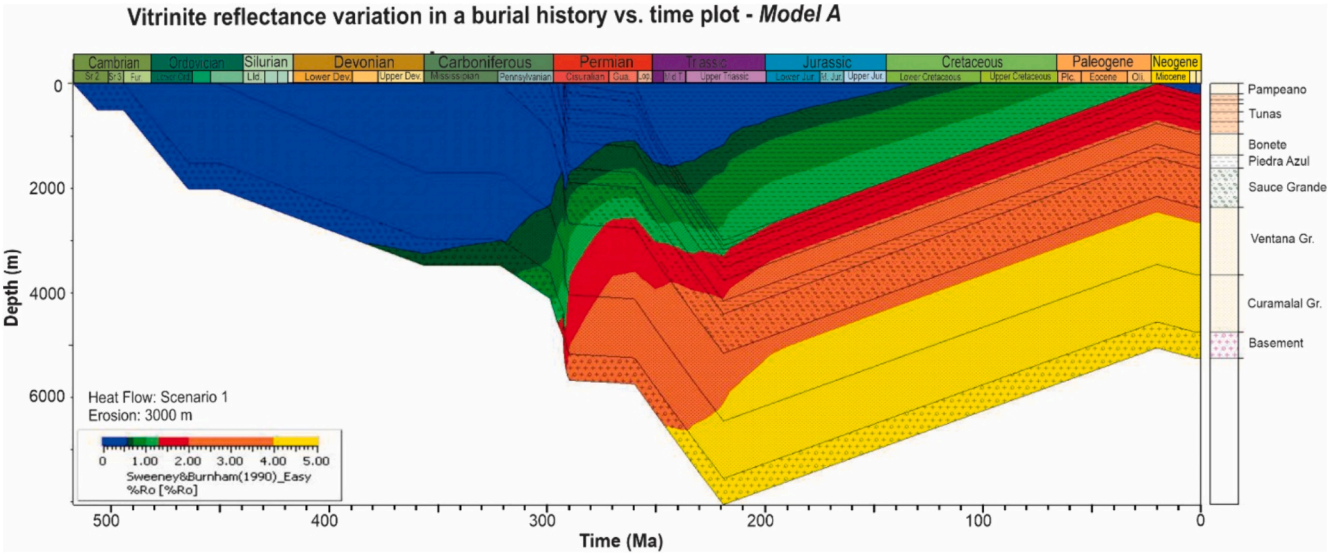

Fig. 13. Vitrinite reflectance variation in a burial vs. time plot for the Tunas Formation (PANG 0001 and PANG 0003 wells) showing the VRo % values over time for the Model A.

geometry and structural elements of the basin and could therefore constrain the distribution and thermal maturity of source rocks along a basin transect, the hydrocarbon migration pathways, and the presence of stratigraphic and structural traps.

6. Summary and concluding remarks

The results obtained by combining geochemical analysis, organic petrology, and thermal modeling techniques provide new insights into the thermal and burial history of the Claromecó Basin and shed light on the tectono-stratigraphic evolution of the southwestern Gondwana margin. Furthermore, a detailed characterization of the coal deposits of the Tunas Formation was attained, which can help to decrease uncertainties in the exploration of potential energy resources in Argentina.

Rock-Eval pyrolysis data show TOC values from 0.13 to 60.35 wt%, with high values (> 20 wt%) belonging to carbonaceous shales and coals. Low HI (< 50 mg HC/g TOC) and OI (< 50 mg CO_2/g TOC) indicate the dominance of Type III and Type IV kerogens, the latter most likely resulting from the thermal maturation of an original Type III kerogen. Geochemical data are consistent with maceral analysis results, which indicate that coals and organic-rich shales are mainly composed of inertinite macerals and minor proportions of vitrinite and liptinite. Tmax values vary between 408 and 608 °C, with most temperatures above 500 °C. Further, low values of HI (< 20 mg HC/g TOC) and Tmax above 500 °C confirm a post-mature stage for the analyzed samples. Vitrinite reflectance values (VRo %) range from 1.50 to 2.0%. Geochemical data combined with VRo % measurements confirm a late catagenesis to metagenesis stage within the wet to dry gas window for coals and organic-rich strata.

Different scenarios were tested for thermal model reconstructions, varying the paleo heat flow and erosion thicknesses (Permian–Cenozoic unconformity), which are the main factors that constrain the thermal history of the basin infill. The best calibration results were obtained with an erosion thickness of 3000 up to 4200 m and paleo heat flow peaks of either 60 or 80 mW/m^2 during the Lower Permian–Lower Cretaceous. The Tunas Formation was deposited and buried during the Permian–-Triassic foreland stage (Gondwanides Orogeny phase). Based on the reconstructed models, this unit attained a maximum temperature of 180 °C at a maximum burial depth of at least 3000 m during the Late Triassic. During the Mesozoic, rifting and drifting events affected the SW margin of Gondwana, resulting in the uplift and exhumation of the Claromecó Basin and the erosion of at least 3000 m of the basin infill, located in the outer part of the extensional system.

The results obtained by combining geochemical analysis, organic petrology, and thermal modeling techniques indicate that the coal beds of the Tunas Formation could have a current potential as gas-prone source rocks. Despite reaching the appropriate coalification degree for gas generation, the current hydrocarbon generation capacity of coals and organic-rich levels is low (S2 < 11 mg HC/g rock, HI < 50 mg HC/g TOC) due to the high percentage of residual kerogen (Type IV) that constitutes the organic fraction. However, since the studied stratigraphic section reached the oil to gas window thermal conditions relatively early in its burial history (Permian-Triassic), the potentially generated hydrocarbons could have been lost due to migration or could be trapped somewhere in the basin if the traps were already present in this early evolution phase of the basin. To improve the understanding of the hydrocarbon potential of the area, further studies are needed that take into account the geometry (2D section or 3D model) and the structural evolution of the basin.

CRediT authorship contribution statement

María Belén Febbo: Writing – original draft, Visualization, Methodology, Investigation, Data curation, Conceptualization. **Silvia Omodeo-Salé:** Writing – review & editing, Validation, Supervision, Methodology, Investigation. **Andrea Moscariello:** Writing – review & editing, Supervision, Funding acquisition.

Declaration of competing interest

The authors declare that they have no known competing financial interests or personal relationships that could have appeared to influence the work reported in this paper.

Data availability

No data was used for the research described in the article.

Acknowledgments

The authors thank the “Department of Earth Sciences” of the University of Geneva, Switzerland, for providing the equipment and personnel to carry out sample analysis. Special thanks to the ’Institute of Geology and Geochemistry of Petroleum and Coal’ of the RWTH Aachen

University for your help in sample preparation. Schlumberger is acknowledged for granting academic licenses of PetroMod to the University of Geneva. The cores were donated to Universidad Nacional del Sur (UNS, Bahía Blanca, Argentina) by Rio Tinto Mining Exploring Company. Special thanks to the two reviewers, Dr. George Siavalas and Dr. Jolanta Kus, for their valuable suggestions and careful corrections of the manuscript, which have improved it considerably.

The author acknowledges the support from the Federal Commission for Scholarships for Foreign Students for the award of the "Swiss Government Excellence Scholarship (ESKAS No. 2022.0445)" that made it possible to performed a research internship in the University of Geneva and the "Consejo Nacional de Investigaciones Científicas y Técnicas (CONICET)" for the Doctoral Scholarship.

References

Alessandretti, L., Philipp, R.P., Chemale, F., Brückmann, M.P., Zvirtes, G., Metté, V., Ramos, V.A., 2013. Provenance, volcanic record, and tectonic setting of the Paleozoic Ventania Fold Belt and the Claromecó Foreland Basin: implications on sedimentation and volcanism along the southwestern Gondwana margin. J. S. Am. Earth Sci. 47, 12–31. https://doi.org/10.1016/j.jsames.2013.05.006.

Allen, P.A., Allen, J.R., 2005. Basin Analysis: Principles and Applications. Blackwell Publishing, Hoboken.

Andreis, R.R., Archangelsky, S., González, C.R., López Gamundi, O., Sabattini, N., Aceñolaza, G., Azcuy, C.L., Cortiñas, J., Cuerda, A., Cúneo, R., 1987. Cuenca tepuel–genoa. In: Archangelsky, S. (Ed.), El Sistema Carbonífero de la República Argentina. Publicación Especial, Academia Nacional de Ciencias, pp. 169–196.

Andreis, R.R., Iñiguez Rodríguez, A.M., Lluch, J.J., Rodríguez, S., 1989. Cuenca paleozoica de Ventania. Sierras Australes de la provincia de Buenos Aires. In: Chebli, G., Spalletti, L. (Eds.), Cuencas Sedimentarias Argentinas, 6. Serie Correlación Geológica, pp. 265–298.

Archangelsky, S., Cúneo, R., 1984. Zonación del Pérmico continental de Argentina sobre la base de sus plantas fósiles. In: 3° Congreso Latinoamericano Paleontológico, pp. 143–153.

Arzadún, G., Tomezzoli, R.N., Cesaretti, N.N., 2016. Tectonic insight based on anisotropy of magnetic susceptibility and compaction studies in the Sierras Australes thrust and fold belt (Southwest Gondwana boundary, Argentina). Tectonics 35, 1015–1031. https://doi.org/10.1002/2015TC003976.

Arzadún, G., Cisternas, M.E., Cesaretti, N.N., Tomezzoli, R.N., 2017. Presence of charcoal as evidence of paleofires in the Claromecó Basin, Permian of Gondwana, Argentina: diagenetic and paleoenvironment analysis based on coal petrology studies. GeoResJ 14, 121–134. https://doi.org/10.1016/j.grj.2017.11.001.

Arzadún, G., Tomezzoli, R.N., Trindade, R., Gallo, L.C., Cesaretti, N.N., Calvagno, J.M., 2018. Shrimp zircon geochronology constrains on Permian pyroclastic levels, Claromecó Basin, south West margin of Gondwana, Argentina. J. S. Am. Earth Sci. 85, 191–208. https://doi.org/10.1016/j.jsames.2018.05.001.

Arzadún, G., Lovecchio, J.P., Becchio, R., Uriz, N.J., Cingolani, C., Febbo, M.B., Hernandez, R., Bolatti, N., Kress, P., 2020. Thermochronology of the Ventana Ranges and Claromecó Basin, Argentina: record of Gondwana breakup and South Atlantic passive margin dynamics. J. S. Am. Earth Sci. https://doi.org/10.1016/j.jsames.2020.1029 in press.

Arzadún, G., Tomezzoli, R.N., Fortunatti, N., Cesaretti, N.N., Febbo, M.B., Calvagno, J. M., 2021. Deformation understanding in the upper Paleozoic of Ventana ranges at Southwest Gondwana boundary. Scientific-Reports 11, 20804. https://doi.org/10.1038/s41598-021-99087-1.

ASTM-D7708–23, 2023. Standard Test Method for Microscopical Determination of the Reflectance of Vitrinite Dispersed in Sedimentary Rocks.

Ballivián Justiniano, C.A., Comerio, M.A., Otero, Geró, Sato, A.M., Coturel, E.P., Naipauer, M., Basei, M.A.S., 2020. Geochemical, palaeontological, and sedimentological approaches of a syn-orogenic clastic wedge: Implications for the provenance of the Permian (Cisuralian) Tunas Formation, Ventania System (Argentina). J. S. Am. Earth Sci. https://doi.org/10.1016/j.jsames.2020.102836 in press.

Bicca, M.M., Kalkreuth, W., da Silva, T.F., de Oliveira, C.H.E., Genezini, F.A., 2020. Thermal and depositional history of Early-Permian Rio Bonito Formation of southern Paraná Basin – Brazil. Int. J. Coal Geol. 228, 103554 https://doi.org/10.1016/j.coal.2020.103554.

Buggisch, W., 1987. Stratigraphy and very low grade metamorphism of the Sierras Australes of the Province of Buenos Aires, Argentina and implications in Gondwana correlations. Zentralb. Mineral. Geol. Paläontol. 1, 819–837.

Burnham, A.K., 2016. Correction to a simple kinetic model of oil generation, vaporization, coking, and cracking. Energy Fuel 30, 2524.

Choque, G., Fortunatti, N.B., Febbo, M.B., Caruso, S., Tomezzoli, R.N., Cesaretti, N.N., 2021. Fracturación estratigráfica en la Formación Tunas (pozo PANG 0003), Cuenca de Claromecó, Buenos aires, Argentina. Rev. Asoc. Geol. Argent. 79, 2.

Choque, G., Fortunatti, N.B., Febbo, M.B., Tomezzoli, R.N., 2022. Fracture frequency and anisotropy of magnetic susceptibility: a case of study in the Claromecó Basin (PANG 0003 well), southwestern Gondwana boundary. J. S. Am. Earth Sci. 120 https://doi.org/10.1016/j.jsames.2022.104094.

Christiansen, R.O., Ballivián Justiniano, C.A., Oriolo, S., Gianni, G.M, García, H.P., Martinez, M.P., Kostadinoff, J., 2021. Crustal architecture and tectonic evolution of the southernmost Río de la Plata Craton and its Neoproterozoic–Paleozoic sedimentary cover: Insights from 3D litho-constrained stochastic inversion models. Precambrian Res., 362, 106307, doi:https://doi.org/10.1016/j.precamres.2021.106307.

De Wit, M.J., Jeffery, M., Bergh, H., Nicolaysen, L., 1988. Geological Map of Sectors of Gondwana, Reconstructed to their Disposition d 150 ma. American Association of Petroleum Geologists, Tulsa, USA.

Di Nardo, J.E., Martínez, M.A., di Pasquo, M., 2022. Lancettopsis harringtonii sp. nov, a new acritarch and related morphotypes from the Sauce Grande Formation of Pennsylvanian-Cisuralian age, Claromecó Basin, Argentina. Rev. Palaeobot. Palynol. 306, 104739 https://doi.org/10.1016/j.revpalbo.2022.104739.

di Pasquo, M., Martínez, M.A., Freije, H., 2008. Primer registro palinológico de la Formación Sauce Grande (Pennsylvaniano-Cisuraliano) en las Sierras Australes, provincia de Buenos Aires, Argentina. Ameghiniana 45 (1), 69–81.

Espitalié, J., Deroo, G., Marquis, F., 1985a. La pyrolyse Rock-Eval et ses applications : Première Partie. Oil Gas Sci. Technol. 40, 563–580.

Espitalié, J., Deroo, G., Marquis, F., 1985b. La pyrolyse Rock-Eval et ses applications: Deuxième partie. Oil Gas Sci. Technol. 40, 755–784.

Espitalié, J., Deroo, G., Marquis, F., 1986. La pyrolyse Rock-Eval et ses applications. Troisième partie. Oil Gas Sci. Technol. 41, 73–89.

Febbo, M.B., Tomezzoli, R.N., Calvagno, J.M., Arzadún, G., Gallo, L., Cesaretti, N.N., 2021. Anisotropy of magnetic susceptibility analysis in Tunas Formation cores (Permian), Claromecó Basin, Buenos Aires, Argentina: its relation to depositional and post-depositional conditions. J. S. Am. Earth Sci. https://doi.org/10.1016/j.jsames.2020.103144 in press.

Febbo, M.B., Arzadún, G., Cesaretti, N.N., Tomezzoli, R.N., Fortunatti, N., 2022a. The Claromecó Frontier Basin: Hydrocarbon source rock potential of the Tunas Formation, southwestern Gondwana margin, Argentina. Mar. Pet. Geol. 137, 105491.

Febbo, M.B., Tomezzoli, R.N., Cesaretti, N.N., Choque, G., Fortunatti, N., Arzadún, G., 2022b. Paleotectonic setting during Permian sedimentation in the Claromecó Foreland Basin, southwestern Gondwana margin (Buenos Aires, Argentina). J. Paleogeogr. 11 (3), 427–447. https://doi.org/10.1016/j.jop.2022.06.001.

Febbo, M.B., Cesaretti, N., Omodeo-Sale, S., Moscariello, A., de Haller, A., Fortunatti, N., Choque, G., Tomezzoli, R., 2023. Diagenetic evolution of the Permian Tunas Formation, Claromec6 Basin, Buenos Aires province, Argentina: its impact on porosity and reservoir characteristics. Latin Am. J. Sedimentol. Basin Anal. 31 (1) (In press).

Fernandes, P., Cogné, N., Chew, D.M., Rodrigues, B., Jorge, R.C., Marques, J., Jamal, D., Vasconcelos, L., 2015. The thermal history of the Karoo Moatize-Minjova Basin, Tete Province, Mozambique: an integrated vitrinite reflectance and apatite fission track thermochronology study. J. Afr. Earth Sci. 112, 55–72. https://doi.org/10.1016/j.jafrearsci.2015.09.009.

Fryklund, B., Marshall, A. and Stevens, J. 1996. Cuenca del Colorado. En Ramos V.A. y Turic M.A. (ed.), Geología y Recursos Naturales de la Plataforma Continental Argentina, Relatorio 8, Asociación Geológica Argentina 135–158, Buenos Aires.

Furque, G., 1965. Nuevos afloramientos del Paleozoico en la provincia de Buenos Aires. Rev. Museo Plata 5, 239–243.

Grasetti, C.G., Piqué, T., Noya, M., Vila, G.S., Manoni, R., Brisson, I., De Leo, D., Dzelalija, D., Canale, N., Zalazar, M., Cabana, C., Tunik, M., Fortunatti, N., Lebinson, F., Bahía, M., Grill, S., 2022. Atlas AR-CO_2. An Argentinian atlas for underground CO 2 storage potential. In: 16th International Conference on Greenhouse Gas Control Technologies, GHGT-16, Lyon, France.

Harrington, H.J., 1947. Explicación de las Hojas Geológicas 33m y 34m, Sierras de Curamalal y de la Ventana, Provincia de Buenos Aires, 61. Servicio Nacional de Minería y Geología, Buenos Aires, p. 43.

Harrington, H.J., 1970. Sierras Australes de Buenos Aires. In: Leanza, A.F. (Ed.), Geología Regional Argentina. Academia Nacional de Ciencias, Córdoba, pp. 395–405.

Heine, C., Zoethout, J., and Müller, R.D., 2013. Kinematics of the South Atlantic rift Solid Earth, 4, 215–253. doi:https://doi.org/10.5194/se-4-215-2013, 2013.

ICCP, 1998. The new vitrinite classification (ICCP system 1994). Fuel 77 (5), 349–358. https://doi.org/10.1016/S0016-2361(98)80024-0.

ICCP, 2001. The new inertinite classification (ICCP system 1994). Fuel 80 (4), 459–471. https://doi.org/10.1016/S0016-2361(00)00102-2.

Introcaso, A., 1982. Características de la Corteza en el Positivo Bonaerense: Tandilia-Cuenca Interserrana-Ventania a Través de Datos de Gravedad. Observatorio Astronómico Municipalidad de Rosario, 8. Publicación del Instituto de Física de Rosario, Rosario, pp. 1–6.

ISO 7404-5, 2009. Methods for the Petrographic Analysis of Coal—Part 5: Methods of Determining Microscopically the Reflectance of Vitrinite. International Organization for Standardization, Geneva, Switzerland, p. 14.

ISO-7004-2, 2009. Methods for the Petrographic Analysis of Coal—Part 2: Methods of Determining Methods of Preparing Coal Samples. International Organization for Standardization, Geneva, Switzerland, p. 12.

ISO-7004-3, 2009. Methods for the Petrographic Analysis of Coal—Part 3: Method of Determining Maceral Group Composition. International Organization for Standardization, Geneva, Switzerland, p. 7.

Keidel, J., 1916. La geología de las Sierras de la provincia de Buenos Aires y sus relaciones con las montañas del Cabo y los Andes. In: Ministerio de Agricultura de la Nación. Sección Geología, Mineralogía y Minería. Anales 9, vol. 3. Buenos Aires, pp. 5–57.

Kollenz, S., Glasmacher, U.A., Rossello, E.A., Stockli, D.F., Schad, S., Pereyra, R.E., 2017. Thermochronological constrains in the Cambrian to recent geological evolution of the argentine passive continental margin. Tectonophysics 716, 182–203.

Kostadinoff, J., 2007. Evidencia geofísica del umbral de Trenque Lauquen en la extensión norte de la cuenca de Claromecó, provincia de Buenos Aires. Rev. Asoc. Geol. Argent. 62 (1), 69–75.
Kostadinoff, J., Prozzi, C., 1998. Cuenca de Claromecó. Rev. Asoc. Geol. Argent. 53 (4), 461–468.
Larson, R., Ladd, J., 1973. Evidence for the opening of the South Atlantic in the early cretaceous. Nature 246, 209–212. https://doi.org/10.1038/246209a0.
Lesta, P., Sylwan, C., 2005. Cuenca de Claromecó. In: VI Congreso de Exploración y Desarrollo de Hidrocarburos, Simposio Frontera Exploratoria de la Argentina. Actas, Mar del Plata, pp. 217–231.
Littke, R., Bayer, U., Gajewski, D., Nelskamp, S., 2008. Dynamics of Complex Intracontinental Basins: The Central European Basin System. Springer, Berlin.
López-Gamundi, O.R., Rossello, E.A., 2021. The Permian Tunas Formation (Claromecó Basin, Argentina): potential naturally fractured reservoir and/or coal bed methane (CBM) play? Mar. Pet. Geol. https://doi.org/10.1016/j.marpetgeo.2021.104998.
López-Gamundi, O.R., Conaghan, P.J., Rossello, E.A., Cobbold, P.R., 1995. The Tunas Formation (Permian) in the Sierras Australes Foldbelt, east Central Argentina: evidence for syntectonic sedimentation in a foreland basin. J. S. Am. Earth Sci. 8 (2), 129–142. https://doi.org/10.1016/0895-9811 (95)00001-V.
López-Gamundi, O.R., Fildani, A., Weislogel, A., Rossello, E., 2013. The age of the Tunas Formation in the Sauce Grande basin-Ventanafoldbelt (Argentina): implications for the Permian evolution of the southwestern margin of Gondwana. J. S. Am. Earth Sci. 45, 250–258.
Lovecchio, J.P., Rohais, S., Joseph, P., Bolatti, N.D., Kress, P.R., Gerster, R., Ramos, V.A., 2018. Multistage rifting evolution of the Colorado basin (offshore Argentina): evidence for extensional settings prior to the South Atlantic opening. Terra Nova 30, 359–368. https://doi.org/10.1111/ter.12351.
Lovecchio, J.P., Rohais, S., Joseph, P., Bolatti, N.D., Ramos, V.A., 2020. Mesozoic rifting evolution of SW Gondwana: a poly-phased, subduction-related, extensional history responsible for basin formation along the Argentinean Atlantic margin. Earth Sci. Rev. 203, 103–138. https://doi.org/10.1016/j.earscirev.2020.103138.
Macdonald, D., Gomez-Perez, I., Franzese, J., Spalletti, L., Lawver, L., Gahagan, L., Dalziel, I., Thomas, C., Trewin, N., Hole, M., Paton, D., 2003. Mesozoic break-up of SW Gondwana: implications for regional hydrocarbon potential of the southern South Atlantic. Mar. Pet. Geol. 20, 287–308. https://doi.org/10.1016/S0264-8172 (03)00045-X.
Magoon, L.B., Dow, W.G., 1994. The petroleum system. In: Magoon, L.B., Dow, W.G. (Eds.), the Petroleum System—From Source to Trap, Vol. 60. AAPG Memoire.
Milani, E.J., De Wit, M.J., 2008. Correlations between the classic Paraná and Cape Karoo sequences of South America and southern Africa and their basin infills flanking the Gondwanides: du Toit revisited. Geol. Soc. Lond. Spec. Publ. 294, 319–342. https://doi.org/10.1144/SP294.17.
Monteverde, A., 1937. Nuevo yacimiento de material pétreo en González Chaves. Rev. Miner. 8, 116–124.
Mpodozis, C., Ramos, V.A., 2008. ectónica jurásica en Argentina y Chile: extensión, subducción oblicua, rifting, deriva y colisiones? Rev. Asoc. Geol. Argent. 63, 4.
Mukhopadhyay, P.K., Wade, J.A., Kruge, M.A., 1995. Organic facies and maturation of Jurassic/Cretaceous rocks, and possible oil-source rock correlation based on pyrolysis of asphaltenes, Scotion Basin,Canada. Org. Geochem. 22, 85–110. https://doi.org/10.1016/0146-6380(95)90010-1.
Nielsen, S., Clausen, O.R., McGregor, E., 2015. Basin% Ro: a vitrinite reflectance model derived from basin and laboratory data. Basin Res. 29, 515–536.
Pángaro, F., Ramos, V.A., 2012. Paleozoic crustal blocks of onshore and offshore Central Argentina: New pieces of the southwestern Gondwana collage and their role in the accretion of Patagonia and the evolution of Mesozoic South Atlantic sedimentary basins. Mar. Pet. Geol. 37 (1), 162–183. https://doi.org/10.1016/j.marpetgeo.2012.05.010.
Pángaro, F., Ramos, V.A., Pazos, P.J., 2015. The Hesperides basin: a continental-scale upper Palaeozoic to Triassic basin in southern Gondwana. Basin Res. 28, 685–711. https://doi.org/10.1111/bre.12126.
Peters, K.E., Cassa, M.R., 1994. Applied source rock geochemistry. In: Magoon, L.B., Dow, W.G. (Eds.), The Petroleum System—from Source to Trap. American Association of Petroleum Geologists, Tulsa, OK, USA, pp. 93–120.
Pickel, W., Kus, J., Flores, D., Kalaitzidis, S., Christanis, K., Cardott, B.J., Misz-Kennan, M.S., Rodrigues, S., Hentschel, A., Hamor-Vido, M., Crosdale, P., Wagner, N., 2017. Classification of liptinite–ICCP system 1994. Int. J. Coal Geol. 169, 40–61. https://doi.org/10.1016/j.coal.2016.11.004.
Prezzi, C.B., Vizán, H., Vázquez, S., Renda, E., Oriolo, S., Japas, M.S., 2018. Evolution of the Paleozoic Claromecó Basin (Argentina) and geodynamic implications for the southwestern margin of Gondwana: Insights from isostatic, gravimetric and magnetometric models. Tectonophysics 742–743, 120–136. https://doi.org/10.1016/j.tecto.2018.05.025.
Ramos, V.A., 1984. Patagonia: Un Nuevo Continente Paleozoico a la Deriva? IX Congreso Geológico Argentino, 2. Actas, Bariloche, pp. 311–325.
Ramos, V.A., 2008. Patagonia: a Paleozoic continental drift? J. S. Am. Earth Sci. 26, 235–251. https://doi.org/10.1016/j.jsames.2008.06.002.
Ramos, V.A., Naipauer, M., 2014. Patagonia: where does it come from? J. Iber. Geol. 40, 367–379. https://doi.org/10.5209/rev_JIGE.2014.v40.n2.45304.
Ramos, V.A., Chemale, F., Naipauer, M., Pazos, P.J., 2014. A provenance study of the Paleozoic Ventania System (Argentina): transient complex sources from Western and Eastern Gondwana. Gondwana Res. 26, 719–740. https://doi.org/10.1016/j.gr.2013.07.008.
Rapela, C.W., Pankhurst, R.J., Fanning, C.M., Grecco, L.E., 2003. Basement evolution of the Sierra de la Ventana Fold Belt: new evidence for Cambrian continental rifting along the southern margin of Gondwana. J. Geol. Soc. Lond. 160, 613–628.
Rapela, C.W., Pankhurst, R.J., Casquet, C., Fanning, C.M., Baldo, E.G., Gonzalez-Casado, J.M., Galindo, C., Dahlquist, J., 2007. The Rio de la Plata craton and the assembly of SW Gondwana. Earth Sci. Rev. 83, 49–82.
Royden, L., 1986. A simple method for analyzing subsidence and heat flow in extensional basins. In: Burrus-Jean (Ed.), Thermal Modeling in Sedimentary Basins. Technip, Paris, pp. 49–73.
Suárez-Ruiz, I., Flores, B., Mendonça Filho, J.G., Hackley, P.C., 2012. Review and update of the applications of organic petrology: part 1, geological applications. Int. J. Coal Geol. 99, 54–112.
Suero, T., 1972. Compilación geológica de las Sierras Australes de la provincia de Buenos Aires. LEMIT (La Plata) 3, 135–147.
Sweeney, J.J., Burnham, A.K., 1990. Evaluation of a simple model of vitrinite reflectance based on chemical kinetics (1). AAPG Bull. 74, 1559–1570.
Taylor, G.H., Teichmuller, M., Davis, A., Diessel, C.F.K., Littke, R., Robert, P., 1998. Organic Petrology. Gebrüder Borntraeger, Berlin, p. 704.
Tissot, B.P., Welte, D.H., 1984. Petroleum Formation and Occurrence. Springer Science & Business Media, Berlin, Germany.
Tissot, B.P., Pelet, R., Ungerer, P.H., 1987. Thermal history of sedimentary basins, maturation indices, and kinetics of oil and gas generation. AAPG Bull. 71 (12), 1445–1466.
Tohver, E., Weil, A.B., Solum, J.G., Hall, C.M., 2008. Direct dating of chemical remagnetizations in sedimentary rocks, insights from clay mineralogy and 40Ar/39Ar age analysis. Earth Planet. Sci. Lett. 274, 524–530.
Tomezzoli, R.N., 2001. Further palaeomagnetic results from the Sierras Australes fold and thrust belt, Argentina. Geophys. J. Int. 147, 356–366. https://doi.org/10.1046/j.0956–540x.2001.01536.x.
Tomezzoli, R.N., 2012. Chilenia y Patagonia: ¿un mismo continente a la deriva? Rev. Asoc. Geol. Argent. 69 (2), 222–239.
Tomezzoli, R.N., Vilas, J.F., 1997. Paleomagnetismo y fabrica magnética en afloramientos cercanos a las Sierras Australes de la Provincia de Buenos Aires (Lopez Lecube y Gonzalez Chaves). Rev. Asoc. Geol. Argent. 52 (4), 419–432.
Tomezzoli, R.N., Tickyj, H., Rapalini, A.E., Gallo, L.C., Cristallini, E.O., Arzadun, G., Chemale Jr., F., 2018. Gondwana's apparent polar wander path during the Permian-new insights from South America. Nat. Sci. Rep. 8, 8436.
Vazquez Lucero, S.E., Prezzi, C., Scheck-Wenderoth, M., Bott, J., Gomez Dacal, M.L., Balestrini, F.I., Vizán, H., 2020. 3D gravity modelling of Colorado and Claromecó Basins: new evidences for the evolution of the southwestern margin of Gondwana. Int. J. Earth Sci. https://doi.org/10.1007/s00531-020-01944-3.
Welte, D.H., Horsfield, B., Baker, D.R., 1997. Petroleum and Basin Evolution: Insights From Petroleum Geochemistry,Geology and Basin Modeling. Springer, Berlin, p. 534.
Williams, K.E., 1995. Tectonic subsidence analysis and Palaeozoic palaeogeography of Gondwana. In: Tankard, A.J., Suarez Soruco, R., Welsink, H.J. (Eds.), Petroleum Basins of South America, 62. American Association of Petroleum Geologists, Memoirs, pp. 79–100.
Withjack, M., Malinconico, M.A., Durcanin, M., 2020. The "passive" margin of eastern North America: rifting and the influence of prerift orogenic activity on postrift development. Lithosphere 29. https://doi.org/10.2113/2020/8876280.
Wygrala, B., 1988. Integrated computer-aided basin modeling applied to analysis of hydrocarbon generation history in a Northern Italian oil field. Org. Geochem. 13, 187–197.
Yu, H., Zhou, G., Fan, W., Ye, J., 2007. Predicted CO2 enhanced coalbed methane recovery and CO2 sequestration in China. Int. J. Coal Geol. 71 (2–3), 345–357.
Zavala, C.A., Santiago, M.F., Amaolo, G.E., 1993. Depósitos fluviales de la Formación Tunas (Pérmico). Cuenca Paleozoica de Ventania, Provincia de Buenos Aires. Rev. Asoc. Geol. Argent. 48 (3–4), 307–316.
Zavala, C., Torresi, A., Zorzano, A., Arcuri, M., Di Meglio, M., 2019. Análisis sedimentológico y estratigráfico de la Formación Tunas (Pérmico, Cuenca de Claromecó). Estudio de subsuelo de los pozos PANG0001 y PANG0003. Rev. Asoc. Geol. Argent. 76 (3), 296–314.